

# The role of AGN in the structure, kinematics and evolution of ETGs in the Horizon simulations

M. S. Rosito<sup>1</sup>, S. E. Pedrosa<sup>2,3</sup>, P. B. Tissera<sup>4,5</sup>, N. E. Chisari<sup>6</sup>, R. Domínguez-Tenreiro<sup>2,7</sup>, Y. Dubois<sup>8</sup>, S. Peirani<sup>8,9</sup>, J. Devriendt<sup>10</sup>, C. Pichon<sup>8,11</sup>, A. Slyz<sup>10</sup>.

<sup>1</sup> Departamento de Matemática. Facultad de Ciencias Exactas y Naturales. Universidad de Buenos Aires. Pabellón I. Ciudad Universitaria C1428EGA Buenos Aires, Argentina.

<sup>2</sup> Departamento Física Teórica, Universidad Autónoma de Madrid, E-28049 Cantoblanco, Madrid, Spain.

<sup>3</sup> Instituto de Astronomía y Física del Espacio, CONICET-UBA. 1428. Buenos Aires, Argentina.

<sup>4</sup> Instituto de Astrofísica, Pontificia Universidad Católica, Av. Vicuña Mackenna 4860, Santiago, Chile.

<sup>5</sup> Centro de Astro-Ingeniería, Pontificia Universidad Católica de Chile, Av. Vicuña Mackenna 4860, Santiago, Chile.

<sup>6</sup> Institute for Theoretical Physics, Utrecht University, The Netherlands, Princetonplein 5, 3584 CC Utrecht, The Netherlands.

<sup>7</sup> Centro de Investigación Avanzada en Física Fundamental, Universidad Autónoma de Madrid, E-28049 Cantoblanco, Madrid, Spain.

<sup>8</sup> Institut d'Astrophysique de Paris, CNRS & Sorbonne Université, UMR 7095, 98 bis Boulevard Arago, 75014, Paris, France.

<sup>9</sup> Université Côte d'Azur, Observatoire de la Côte d'Azur, CNRS, Laboratoire Lagrange, Bd. de l'observatoire, 06304 Nice, France.

<sup>10</sup> Department of Physics, University of Oxford, Keble Road, Oxford OX1 3RH, United Kingdom.

<sup>11</sup> Korea Institute for Advanced Study, 85 Hoegiro, Dongdaemun-gu, Seoul, 02455, Republic of Korea.

December 22, 2024

## ABSTRACT

**Context.** It is well-known that feedback processes play a fundamental role in the regulation of star formation (SF) and, in particular, in the quenching of early-type galaxies (ETGs) as have been inferred by numerical studies of  $\Lambda$ -CDM universe models. At the same time, ETGs are subject to certain fundamental scaling relations, but the connection between them and the physical processes that effect ETG evolution remain unknown.

**Aims.** This work aims at studying the impact of the energetic feedback due to active galactic nuclei (AGN) in the formation and evolution of ETGs. Especially, we assess to what extent modelling AGN feedback is necessary to reproduce observational constraints such as morphology, kinematics and the evolution of the main scaling relations.

**Methods.** The Horizon-AGN and Horizon-noAGN cosmological hydrodynamical simulations were performed with identical initial conditions and including the same physical processes with the exception of the AGN feedback in the former. We select a sample of ETGs from both simulations using the same criteria and subject them to an exhaustive study regarding SF activity, kinematics and scaling relations.

**Results.** We find that galaxies from Horizon-AGN follow observed fundamental scaling relations (mass–plane, Fundamental Plane, mass–size relation) and reproduce, qualitatively, kinematic features such as the bimodality in the spin parameter distribution at  $z = 0$ . The specific star formation activity is within observed ranges when AGN is turned on. Instead, galaxies formed in absence of AGN feedback show differences with observations such as the departure from the Fundamental Plane (FP) of a group of galaxies that have an excess of stellar surface density, and a shallower mass–size relation populated by galaxies with young stellar ages. Interestingly, the mass–plane is found to be less affected by AGN activity. In addition, we study the evolution of the fundamental relations with redshift, finding a mild evolution for  $z < 1$  of the mass–plane in agreement with previous works whereas a slightly stronger change is detected for  $z > 1$  in Horizon-AGN. ETGs in Horizon-noAGN show a weak systematic evolution of the mass–plane. The FP of Horizon-AGN is in agreement with observations at  $z = 0$  and there is no clear trend of evolution. The plane is tight from  $z = 3$  onwards, with a scatter of  $\sim 0.06$  dex. At all analyzed redshifts, when AGN feedback is switched off, a fraction of galaxies departs from the expected FP due to a higher surface stellar density. Overall, the role of AGN feedback on the regulation of the star formation activity have an impact on the size, stellar surface density, stellar ages and masses of ETGs that is reflected in the fundamental relations and the amount of rotation. Its impact could be unveiled from the evolution of evolution of the FP and its dependence on stellar age and galaxy morphology.

**Key words.** galaxies: elliptical and lenticular, cD - galaxies: evolution - galaxies: fundamental parameters - galaxies: kinematics and dynamics

## 1. Introduction

In the current cosmological paradigm, it is known that a number of complex processes, such as major and/or minor mergers, secular evolution and other interactions or environmental effects, contribute to shape the morphology of galaxies (e.g. Tissera et al. 2012; Avila-Reese et al. 2014; Somerville & Davé

2015; Rodriguez-Gomez et al. 2016; Dubois et al. 2016, and references therein), and particularly elliptical or ETGs.

The general picture for ETG formation involves different scenarios that can explain the observed variety in this kind of galaxies (e.g. Kormendy 2016). Analytical models (Soler et al. 2020), as well as N-body simulations (Wechsler et al. 2002; Zhao et al. 2003), have shown that two different phases can

be distinguished along halo mass assembly: first, a violent, fast phase, with high-mass aggregation rates (i.e., merger rates); and later on, a slow phase, where the mass aggregation rates are much lower. Hydrodynamical simulations have confirmed this scenario and its implications for properties of massive galactic objects at low  $z$  (e.g. Domínguez-Tenreiro et al. 2006; Oser et al. 2010; Cook et al. 2009; Domínguez-Tenreiro et al. 2011). Conversely, Naab (2013) proposes two phases: first, in-situ SF at high redshift, and secondly, minor mergers that allow the accretion of stars from other galaxies at later stages. More recently, Clauwens et al. (2018) distinguish three different phases as a function of stellar mass, instead of redshift, in galaxies from EAGLE simulation (Crain et al. 2015; Schaye et al. 2015). These authors conclude that, when galaxies are less massive, they grow due to in-situ SF caused partially by mergers, and present random stellar motion. In an intermediate mass range, galaxies are mostly disc-dominated. Finally, at high masses, galaxies turn more spheroidal and in-situ SF becomes less important.

Feedback processes are essential to regulate the SF, and therefore explain the quenching of ETGs (e.g. Burkert 2004; Hayward & Hopkins 2016; Dubois et al. 2016). Previous works highlight the need for efficient feedback by supernova (SN) and AGN (e.g. Rosito et al. 2018; Starkenburg et al. 2019; Rosito et al. 2019b) to better regulate the star formation activity in numerical simulations. In particular, AGN feedback has been considered relevant only in massive galaxies (see e.g. Somerville & Davé 2015; Rosas-Guevara et al. 2016). Nevertheless, this fact is questioned by recent observational works (Argudo-Fernández et al. 2018; Manzano-King et al. 2019). The latter find AGN activity in dwarf galaxies from SDSS-DR7 and DR8 in the stellar mass range  $[0.6, 9] \times 10^9 M_\odot$ . Therefore, the impact of AGN feedback has to be, at least, re-assessed for low-mass galaxies.

Elliptical galaxies are supported by velocity dispersion and, therefore, the spheroid is the dominant component. However, the amount of rotation of ETGs varies, with fast rotators notably more frequent than slow rotators (Emsellem et al. 2011). A more complete ETGs kinematic classification is summarised in Cappellari (2016) demonstrating that the rotational component plays a non-negligible role in ETG structure. The importance of rotation in elliptical galaxies can also be seen in cosmological simulations as shown in Oñorbe et al. (2007) who find clear rotation curves in some ETGs. Rosito et al. (2018) and Rosito et al. (2019b) analyse the presence of a disc component in the inner region of ETGs coexisting with the bulge, identified in simulations of the Fenix project (Pedrosa & Tissera 2015) and the EAGLE project (Crain et al. 2015; Schaye et al. 2015), respectively. These authors find a strong anti-correlation between the presence of this so-called inner disc and the bulge-to-total stellar mass ratio ( $B/T$ ). This suggests that the disc components of galaxies with low values of  $B/T$ , i.e., more disc dominated, can extend to the central regions, besides having larger radii. In the papers mentioned above (Rosito et al. 2018, 2019b), they measure quantitatively the fraction of these inner disc relative to the bulge mass finding that it can be related to the bulge Sérsic index (Sérsic 1968) and, therefore to their formation histories (Kormendy 2016). In both works, a large variety of fractions of the inner discs are detected which is also related to different relative behaviours of the surface density profiles of the bulge and the inner disc components. The different mass distributions could be the result of different formation histories.

Another remarkable feature of ETGs is that they obey clear scaling relations. The fundamental plane (FP Faber et al. 1987; Dressler et al. 1987; Djorgovski & Davis 1987) links size, velocity dispersion and luminosity, and thus can be expressed in

terms of average surface brightness (e.g. Mo et al. 2010). Under some assumptions, such as homology and constant mass-to-light ratio ( $M/L$ ), that important relation can be derived from the virial theorem (e.g. Binney & Tremaine 1987). However, the observed parameters of this plane are tilted from the virial predictions (e.g. Bernardi et al. 2003; Hyde & Bernardi 2009; Cappellari et al. 2013a; Saulder et al. 2013). This tilt has been a matter of controversy, which has fostered different explanations. For instance, the variation of the  $M/L$  (Faber et al. 1987), the non-homology in the surface brightness distribution (e.g. Prugniel & Simien 1997; Graham & Colless 1997; Bertin et al. 2002; Trujillo et al. 2004), or the variation in the fraction of dark matter (e.g. Renzini & Ciotti 1993; Ciotti et al. 1996; Borriello et al. 2003). Cappellari (2016) emphasises that there is no tilt when the surface brightness is replaced by the dynamical mass, recovering thus the virial relation. Based on hydrodynamical simulations in a cosmological context, Oñorbe et al. (2005) and Oñorbe et al. (2006) analyse the FP of massive galaxies finding a tilt from the virial parameters at galactic scale, while at halo scale virial relations hold. These authors report that the tilt, originated at high redshift (Oñorbe et al. 2011) and showing only a mild evolution after  $z \sim 1.5$  (Domínguez-Tenreiro et al. 2006), is presumably due to a spatial homology breaking associated to a systematic decrease, with increasing galaxy mass, of the relative amount of dissipation experienced by the baryonic mass component during mass assembly (see also Taranu et al. 2015). Recently Lu et al. (2020) present the analysis of the fundamental relations for The Next Generation Illustris Simulations (IllustrisTNG; Marinacci et al. 2018; Naiman et al. 2018; Nelson et al. 2018; Pillepich et al. 2018; Springel et al. 2018) finding a FP that shows a mild evolution and a mass–plane relation in place with small scatter ( $\sim 0.08$  dex) since  $z = 2$ .

Using data from MaNGA survey, Li et al. (2018) report that the evolution of the stellar populations (SPs) results in variations of properties such as mean age and metallicity across the mass–size plane, another scaling relation. Rosito et al. (2019a) study this relation for a sample of galaxies with a large variety of morphologies selected from the EAGLE project. These authors find that at a given stellar mass, mass-weighted ages are younger for more extended ETGs. Additionally, ETGs with small sizes tend to have shallow or positive age gradients. The angular momentum distribution across the mass–size plane is also analysed by Rosito et al. (2019a) who find that for a fixed value of the spin parameter more massive galaxies are more extended. In particular, they report a bimodality in the  $\lambda-\epsilon$  plane with galaxies in the first peak populated by fast rotators with younger SPs and in the second one, by slow rotators with older SPs, in agreement with observational works (Graham et al. 2018).

The main goal of the present work is to analyse the role of the AGN feedback in ETGs using simulations that allow us to isolate the effects of this process. Our study focuses on unveiling the role of AGN feedback on SF regulation, fundamental scaling relations and kinematic parameters. For this purpose, we analyse two simulations from the Horizon project (Dubois et al. 2014; Kaviraj et al. 2017) which share the same initial conditions and subgrid physics except for the AGN feedback: Horizon-AGN and Horizon-noAGN (Peirani et al. 2017, i.e. no AGN feedback is modeled). Several results have been already reported using the Horizon Project which are relevant to our work. Dubois et al. (2016) remark on the importance of simulating AGN feedback to reproduce properly the morphology of galaxies, especially of the massive ones. Furthermore, they conclude that the assembly of ETGs is mostly driven by mergers, having higher fractions of ex-situ stars than disc dominated galaxies, and that the quenching,

regulated by AGN feedback, freezes the resultant morphology triggered by those mergers. Also, by isolating the effect of AGN feedback, Beckmann et al. (2017) compare the stellar mass ratios of twin galaxies from these simulations, i.e., they cross-identify individual galaxies from both simulations, analysing thus the impact of AGN feedback on quenching as a function of stellar mass: smaller galaxies quench at higher redshifts than the massive ones. Massive ETGs are also studied by Peirani et al. (2019), who find that AGN feedback plays a fundamental role to achieve an agreement with observational trends, in particular, they focus on the mass-weighted density slope (Dutton & Treu 2014) and its correlation with other galaxy features, such as mass and effective radius. Recently van de Sande et al. (2019) find that Horizon-AGN galaxies are larger at a given stellar mass than those observed in SAMI galaxy survey (Croom et al. 2012; Bryant et al. 2015), ATLAS<sup>3D</sup> project (Cappellari et al. 2011), CALIFA survey (Sánchez et al. 2012) and MASSIVE survey (Ma et al. 2014).

This paper is organised as follows. In Section 2, we describe the simulations and the criterion to obtain the analysed sample of ETGs and their morphological components is described in Section 3. In Section 4 the characteristics of the simulated ETGs are analysed at  $z = 0$ . The evolution of the fundamental relation parameters is studied in Section 5 and these results are discussed in Section 6. Section 7 summarises our findings.

## 2. Horizon-AGN and Horizon-noAGN simulations

The Horizon simulations are cosmological hydrodynamical simulations consistent with a  $\Lambda$ -CDM universe with  $\Omega_m = 0.272$ ,  $\Omega_\Lambda = 0.728$ ,  $\Omega_b = 0.045$ ,  $H_0 = 100 \text{ km s}^{-1} \text{ Mpc}^{-1}$  being  $h = 0.704$ , and the normalisation of the power spectrum  $\sigma_8 = 0.81$  (Dubois et al. 2014). These parameters are consistent with a WMAP cosmology (Komatsu et al. 2011). The simulated box size is  $100 h^{-1} \text{ Mpc}$  per side with  $1024^3$  dark matter particles of  $8 \times 10^7 \text{ M}_\odot$  (Dubois et al. 2014).

These simulations are run with the RAMSES code (Teyssier 2002) which is based on the adaptative mesh refinement technique (AMR). The initial mesh is refined down to  $\Delta x = 1 \text{ kpc}$ . This refinement is developed by means of a quasi-Lagrangian method: if the number of dark matter particles in a cell exceeds eight, or the total baryonic matter inside the cell is eight times greater than the dark matter resolution, a new refinement is performed. Furthermore, the minimum size of the cells in physical units (taking into account the scale factor) remains approximately constant. The initial conditions are computed using the MPGRAFIC code (Prunet et al. 2008).

Gas cooling processes (including hydrogen, helium and some metals) are described following Sutherland & Dopita (1993) model. Cooling down to  $10^4 \text{ K}$  is allowed. On the other hand, gas heating occurs after reionisation ( $z \sim 10$ ) and is modeled with a UV background following Haardt & Madau (1996). Star formation takes place when the gas density is greater than  $0.1 \text{ H cm}^{-3}$  and is produced randomly (Rasera & Teyssier 2006; Dubois & Teyssier 2008). Such process follows a Schmidt law:  $\dot{\rho}_* = \epsilon_* \rho_g / t_{\text{ff}}$ , where  $\dot{\rho}_*$  is the star formation rate (SFR) density,  $\rho_g$  is the gas density,  $t_{\text{ff}}$  the gas local free-fall time and  $\epsilon_* = 0.02$  is a constant (Kennicutt 1998; Krumholz & Tan 2007). The stellar mass resolution is  $2 \times 10^6 \text{ M}_\odot$  and a Salpeter initial mass function (IMF) is assumed (Salpeter 1955). The simulations also include SNIa and SNII feedback (Dubois et al. 2014). Gas metallicity is modified by galactic winds and the enriched gas is ejected during a SN event. The following elements are modelled: O, Fe, C, N, Mg and Si (Dubois et al. 2014).

Individual galactic structures are identified using the AdaptaHOP code (Aubert et al. 2004) updated by Tweed et al. (2009). In the original galaxy catalog, only objects resolved with more than 50 stellar particles are considered, yielding 150000 galaxies at  $z = 0$ . In the present work, we apply a more restrictive minimum particle number by requesting simulated galaxies to have more than 5000 stellar particles in order to be able to properly resolve galaxies and the evolution with redshift of their fundamental relations.

In the case of Horizon-AGN, black holes are created in regions with gas density higher than a fixed threshold and have an initial mass of  $10^5 \text{ M}_\odot$ . Black holes are not allowed to form within small distances from each other (less than 50 kpc). The accretion rate ( $\dot{M}_{\text{BH}}$ ) and Eddington accretion rate ( $\dot{M}_{\text{Edd}}$ ) are calculated as in Dubois et al. (2012). There are two AGN feedback modes implemented according to the quotient  $\chi = \dot{M}_{\text{BH}} / \dot{M}_{\text{Edd}}$ . If  $\chi < 0.01$ , the situation corresponds to a "radio" mode, otherwise, to a "quasar" mode (Merloni & Heinz 2008). The fraction of energy released by the black hole is assumed to be a free parameter that depends on the mode. Despite the calibration of Horizon-AGN enforcing the  $M_{\text{BH}} - \sigma$  relation, there is evidence that the gas fractions inside haloes are higher than those observed (Chisari et al. 2018). Thus, the results of our work can be assumed to be conservative in gauging the impact of AGN feedback.

These models reproduce a number of black holes observational constraints, such as the black hole mass function and relations between these objects and galaxy properties (Volonteri et al. 2016). There are, however, some differences between these mock objects with the observed ones. In particular, the faint end of the luminosity function is overestimated in the presence of massive black holes at  $z \sim 0.5 - 2$ , which is a common problem in cosmological simulations (Sijacki et al. 2015). A complete analysis of Horizon-AGN black holes can be found in Volonteri et al. (2016) where the authors propose a stronger SN feedback to improve the reproduction of the observational trends. On the other hand, Beckmann et al. (2017) find a relation between the mass of the smallest galaxy affected by AGN feedback with redshift for Horizon-AGN galaxies that is in agreement with observations (Baldry et al. 2004; Peng et al. 2010).

## 3. Sample of galaxies

For our study, we select central galaxies defined as the main one within a virial radius (satellites galaxies are not considered in this work) which are resolved with more than 5000 stellar particles in both simulations. At  $z = 0$ , for Horizon-AGN our galaxy catalog has 17408 members with stellar masses between  $1.3 \times 10^{10}$  and  $1.43 \times 10^{12}$ , whereas, for Horizon-noAGN we find 19466 galaxies with masses varying between  $1.4 \times 10^{10} \text{ M}_\odot$  and  $10^{12.5} \text{ M}_\odot$ . In the case of Horizon-noAGN, we remove 60 galaxies with stellar masses greater than  $10^{12.5} \text{ M}_\odot$  because of their unrealistic properties. The importance of AGN feedback in reproducing the high mass end of the galaxy stellar mass function was previously noted by Beckmann et al. (2017) and is consistent with the fact that AGN feedback prevents excessive SF and in its absence, more massive galaxies can be formed.

To quantify the size of galaxies, we define the optical radius ( $R_{\text{opt}}$ , Tissera et al. 2012) as the 3D radius that encloses  $\sim 80$  per-cent of the stellar mass (first estimated within 100 kpc) and the 3D half-mass radius ( $R_{\text{hm}}$ ) defined as the one which encloses 50 per-cent of the total stellar mass, which is defined as the total stellar mass within  $R_{\text{opt}}$ . Taking into account that maximum

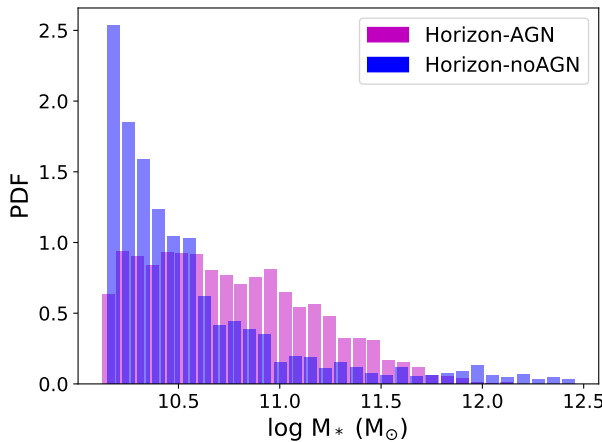


**Fig. 1.** Stellar mass distributions for the selected samples at  $z = 0$  of ETGs from Horizon-AGN (magenta) and Horizon-noAGN (blue). The differences show that in the absence of AGN feedback there are few massive ETGs. We remark the existence of a small tail of massive galaxies in Horizon-noAGN, that may be a result of the lack of AGN feedback.

mesh size resolution, galaxies with  $R_{\text{hm}}$  lower than 2 kpc are not considered.

We note that galaxies are identified at each analysed  $z$  following the same criteria. Galaxies are not followed along their merger tree.

### 3.1. Morphological decomposition

In order to distinguish ETGs from late-type galaxies (LTGs), we follow Chisari et al. (2015) who fix a threshold for  $V/\sigma$  parameter, being  $V$  the tangential (or rotational) velocity and  $\sigma$  the 3D (or the total) velocity dispersion as defined by Dubois et al. (2014). Chisari et al. (2015) fix that threshold at  $V/\sigma = 0.55$ , and therefore, galaxies with  $V/\sigma < 0.55$  are considered ETGs since their rotation is less important. By applying this criterion, the size of the sample of ETGs in Horizon-AGN is 4370, and in Horizon-noAGN, 1560 at  $z = 0$ .

In Fig. 1 we show the stellar mass distributions for both samples. The histograms are, hereafter, normalised so that their enclosed area is 1 approximating, thus, a probability density function (pdf). This allows a direct comparison of the involved quantities. The number of well-resolved, and therefore more massive, galaxies from Horizon-AGN is remarkably larger than those from Horizon-noAGN. This difficulty to form massive elliptical galaxies in absence of AGN feedback is in agreement with the results of Dubois et al. (2016). There is, however, a small tail of very massive ETGs (2.4 per-cent) in the stellar mass distribution of the Horizon-noAGN sample having total stellar masses greater than  $10^{12} M_{\odot}$ .

### 3.2. Inner stellar discs

As reported in Rosito et al. (2018) using the Fenix sample and Rosito et al. (2019b) with the EAGLE sample, there is a rotational component embedded within the bulge, so-called inner stellar discs. In this subsection we inspect the presence of this component in the Horizon galaxies. We measure quantitatively the amount of rotation for each individual stellar particle, by defining locally a parameter  $\sigma/V$  (see Appendix C for a detailed description). The disc particles are those with  $0 < \sigma/V < 1$ .

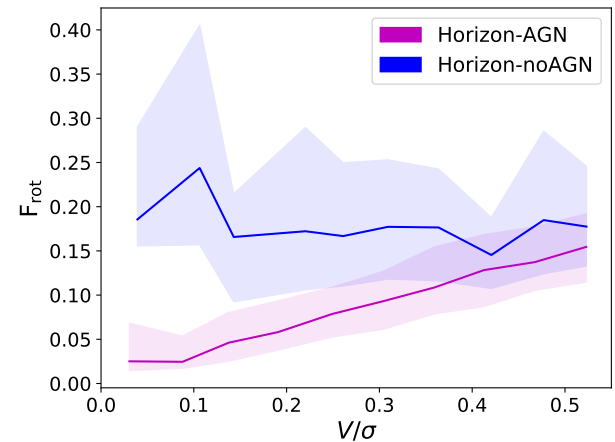


**Fig. 2.**  $F_{\text{rot}}$  as a function of  $V/\sigma$  for ETGs from Horizon-AGN (magenta) and Horizon-noAGN (blue) simulations. The 25 and 75 percentiles are depicted by the shaded regions.

The bulge is defined by stars with  $|\sigma/V| > 1$  within the region enclosed by  $0.5R_{\text{hm}}^1$ . We calculate  $F_{\text{rot}}$  as the ratio of the disc stellar mass ( $0 < \sigma/V < 1$ ) within  $0.5R_{\text{hm}}$ , and the bulge stellar mass. We discard galaxies with inner discs resolved with less than 250 star particles in order to mitigate numerical effects. With this condition, sub-samples comprising 1262 and 345 members are defined for Horizon-AGN and Horizon-noAGN, respectively.

As can be seen from Fig. 2, for ETGs in Horizon-AGN, there is a clear correlation between  $F_{\text{rot}}$  and the globally measured  $V/\sigma$  (as in Dubois et al. 2014) with a p-value  $\sim 0$ . This is consistent with the results of Rosito et al. (2018) and Rosito et al. (2019b) where anti-correlations between  $F_{\text{rot}}$  and  $B/T$  are also reported. For galaxies in Horizon-noAGN, no clear correlation is found (Spearman correlation coefficient  $\sim 0.06$  and p-value  $\sim 0.30$ ).

In Fig. 3, normalised histograms of  $F_{\text{rot}}$  for our sub-samples (Horizon-AGN and Horizon-noAGN ETGs) are shown. For comparison the distribution obtained by Rosito et al. (2019b) for the largest volume run of the EAGLE project simulations is included. It can be seen that the peaks of the distributions for Horizon-AGN and EAGLE ETGs are close to each other, but the latter is significantly higher while the former has larger fraction of ETGs with negligible inner rotation. Horizon-noAGN galaxies present larger values of  $F_{\text{rot}}$ , as can be seen in the same figure. This suggests that AGN feedback can reduce the formation of inner discs and hence, the inner regions are more dispersion-dominated.

## 4. Characterisation of Horizon ETGs at $z = 0$

### 4.1. Star formation activity

By isolating the effect of AGN feedback via the analysis of the Horizon simulations, Beckmann et al. (2017) conclude that this process is crucial to quench galaxies, being the more massive ones ( $M_* > 10^{11} M_{\odot}$ ) the more affected by AGN feedback. In their work, they compare individual galaxies matched between Horizon-AGN and Horizon-noAGN, following their evolution with redshift. They highlight the impact of AGN feedback in

<sup>1</sup> We note that this definition is different from that employed by Rosito et al. (2018) and Rosito et al. (2019b). In those works, the bulge particles are defined as the ones without ordered rotation and most gravitationally bound.

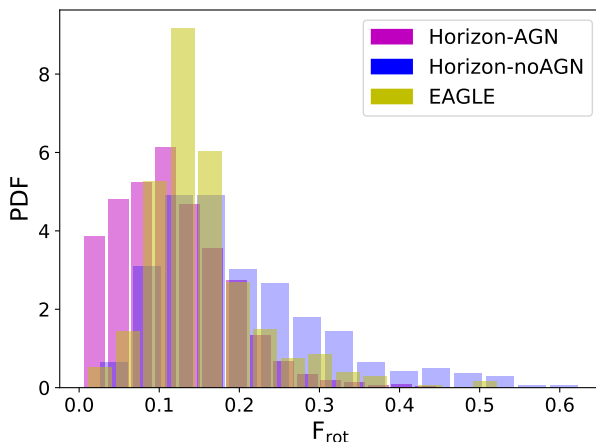


**Fig. 3.** Histograms of  $F_{\text{rot}}$  for ETGs selected from Horizon-AGN (magenta), Horizon-noAGN (blue) and EAGLE (yellow).

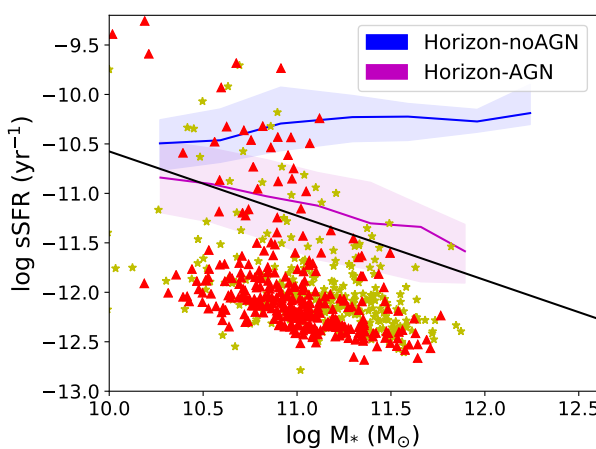


**Fig. 4.** sSFR as a function of stellar mass for ETGs from Horizon-AGN (magenta) and from Horizon-noAGN (blue). The 25 and 75 percentiles are depicted by the shaded region. We include the line separating active and passive galaxies (above and below the line, respectively) reported by Lacerna et al. (2014) and observations of isolated ETGs from UNAM-KIAS catalog (yellow stars Hernández-Toledo et al. 2010) and galaxies in Coma cluster (red triangles Gavazzi et al. 2003).

regulating the SF in galaxies of different morphologies as a result of both the decrease of total gas due to outflows, and the difficulty to accrete gas.

In this work, we analyse the relation between specific star formation rate at  $z = 0$  (sSFR defined as  $\text{SFR}/M_*$ , where the SFR is calculated with stars younger than 0.5 Gyr<sup>2</sup>) and stellar mass for our samples of ETGs from which we can verify the action of AGN. For comparison, we include observations of isolated elliptical galaxies from UNAM-KIAS catalog (Hernández-Toledo et al. 2010) and a sample of galaxies in Coma cluster (Gavazzi et al. 2003). We also consider the criterion reported by Lacerna et al. (2014) to distinguish active and passive galaxies.

As can be seen from Fig. 4, ETGs from Horizon-AGN show a decreasing sSFR for increasing stellar mass, in agreement with observations albeit still more active. A similar result is found for

galaxies from Illustris, for which feedback does not seem enough to suppress SF, as reported in Genel et al. (2014).

On the other hand, ETGs from Horizon-noAGN are, as expected, significantly more star forming with median sSFR which are almost independent of stellar mass, as can be seen in Fig. 4. It must be noticed, however, that in this simulation, SN feedback is not tuned to act alone (the only difference with Horizon-AGN is the lack of black holes formation) and, hence, the differences with observations might be overestimated. In fact, galaxies from the Fenix simulation, which does not include AGN feedback but has been performed with a SN feedback model that reproduce the angular momentum content and the mass-size relation (Pedrosa & Tissera 2015), show a clear trend between sSFR and stellar mass as reported by Rosito et al. (2018). These findings suggest that this scaling relation can be used to calibrate the feedback mechanisms in order to reproduce them as pointed out in previous results for other simulations (e.g. Genel et al. 2014; Vogelsberger et al. 2014b,a, report the need for stronger feedback mechanisms in Illustris simulation).

## 4.2. Mass-size relation

In this Section, we investigate possible dependencies of the mass-size relation on age and level of rotation ( $V/\sigma$ ) of the SPs. We compare the mass-size relation obtained from Horizon-AGN and Horizon-noAGN samples. We use an implementation in Python coded by Cappellari et al. (2013b) of the two-dimensional Locally Weighted Regression method (Cleveland & Devlin 1988) so as to obtain smoothed distributions. See Appendix A for the non-smoothed version of these figures.

### 4.2.1. Galaxies formed under the action of AGN feedback

Let us first study the mass-size relation as a function of  $V/\sigma$  and age. Here, following Rosito et al. (2019a) and Li et al. (2018), we focus on mass-size relation using the dynamical mass,  $M_{\text{dyn}}$ , estimated assuming virialisation ( $M_{\text{dyn}} = \frac{5}{3G}\sigma^2 R_{\text{hm}}$ , being  $G$  the universal gravitational constant). Dubois et al. (2016) already report a strong correlation between stellar mass and the effective radius. Hence, the relation is also present between  $M_{\text{dyn}}$  and  $R_{\text{hm}}$ , as can be seen from Fig. 5. We note that van de Sande et al. (2019) find that galaxies from Horizon-AGN are more extended for all stellar masses than those observed, as mentioned in the introduction.

In Fig. 5 (upper panel) a correlation between mass and  $V/\sigma$  is found, such that more massive galaxies are more dispersion-dominated. This is the expected trend, considering that galaxies with lower level of rotation are, generally, more massive, as reported in observational works (e.g. Emsellem et al. 2011). This is also consistent with the observational results in Li et al. (2018): more massive galaxies present higher values of  $\sigma$ . However, in their work there is little dependence of velocity dispersion on radius. In our sample, since the increase of  $R_{\text{hm}}$  with mass is almost linear, and the correlation is, therefore, stronger,  $V/\sigma$  decreases significantly with increasing size, as well as with mass.

With respect to age variations across the mass-size relation, from the bottom panel of Fig. 5, it is clear that at higher masses, galaxies are dominated by older SPs. From that figure, a very low number of old, low-mass galaxies can be seen but it is not representative of the whole sample.<sup>3</sup> This small less massive old

<sup>2</sup> We did not use an “instantaneous” measure of the SF activity to avoid numerical noise due to the low number of very young particles. See Rosito et al. (2018) and Rosito et al. (2019b).

<sup>3</sup> In some cases, the smoothing methods can be misleading and hence we include in Appendix A the non-smoothed distributions. As regards Fig. A.1 (left panel), this trend of low mass old galaxies cannot be seen.

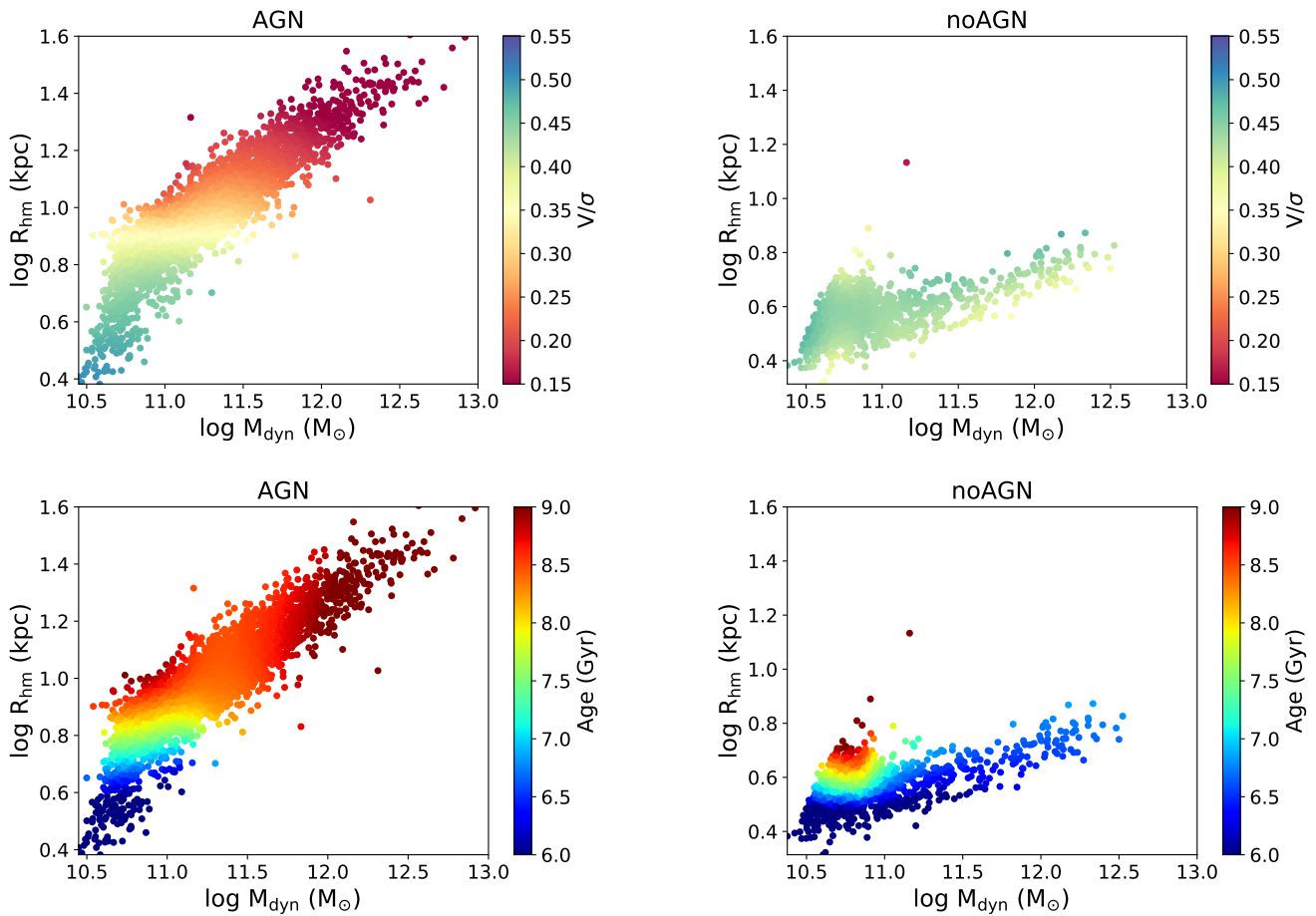


**Fig. 5.** Mass–size relation as a function of  $V/\sigma$  (top panel) and mass-weighted average stellar age (bottom panel) for Horizon-AGN sample of ETGs.

population cannot be seen in the non-smoothed distribution (see Fig. A.1 of Appendix A) and we can therefore conclude that this trend is due to the smoothing method. Our results are consistent with the ones from van de Sande et al. (2019).

#### 4.2.2. Galaxies formed in absence of AGN

The mass–size relation for galaxies formed in absence of AGN feedback shows that those galaxies have lower radii at a given  $M_{\text{dyn}}$ , as seen in Fig. 6. As mentioned in the introduction, it can be clearly seen that the presence of AGN feedback produces more extended galaxies (Dubois et al. 2013). This is consistent with the fact that Horizon-noAGN ETGs present high values of the average surface density,  $\Sigma_e = M_*/(2\pi R_{\text{hm}}^2)$ , with a maximum  $\Sigma_e \sim 10^{10.2} \text{ M}_\odot \text{ kpc}^{-2}$ . In contrast, the maximum  $\Sigma_e$  for ETGs in Horizon-AGN is  $\sim 10^9 \text{ M}_\odot \text{ kpc}^{-2}$ . This fact was previously reported by Peirani et al. (2019), who conclude that without AGN feedback, simulated galaxies are more compact than observed ones, whereas the values of  $\Sigma_e$  for massive ellipticals from Horizon-AGN match the observational data. Nevertheless, they remark that low-mass ETGs from that simulation are not compact enough to be in agreement with observations. We will return to this point in Section 5.

The trend of rotation across mass–size relation is less clear, but massive galaxies still show lower values of  $V/\sigma$  (Fig. 6), as expected. For the age, an old low-mass population can be found

**Fig. 6.** Mass–size relation as a function of  $V/\sigma$  (top panel) and mass-weighted average stellar age (bottom panel) for the Horizon-noAGN sample of ETGs.

but it cannot be attributed to the smoothing method as seen in Fig. A.2. This fact may be ascribed to the action of SN feedback, that is stronger for small galaxies (Larson 1974; White & Rees 1978; Dekel & Silk 1986; White & Frenk 1991), and therefore would quench SF in these objects at earlier times. When the AGN feedback is on, the regulation of the SF is clearly different across the whole mass range so a smoother variation of the mean age is achieved as a function of mass as shown in Fig. 5.

Considering that the SN feedback in this simulation has not been tuned to achieve a better modeling of galaxy properties on its own (i.e. it is the same that is used when the AGN feedback is active), a good match with observations is not to be expected.

#### 4.3. Slow and fast rotators

As in many observational works (e.g. Emsellem et al. 2011), we find that most Horizon-AGN ETGs are fast rotators (see also van de Sande et al. 2019). This is assessed using the spin parameter  $\lambda$  within  $R_{\text{hm}}$  calculated by (e.g. Emsellem et al. 2011; Lagos et al. 2018):

$$\lambda = \frac{\langle R | V | \rangle}{\langle R \sqrt{V^2 + \sigma^2} \rangle},$$

where  $V$  and  $\sigma$  are the tangential velocity and the velocity dispersion averaged along the line-of-sight, respectively, and  $R$  the three-dimensional radius, for consistency with the calculation of

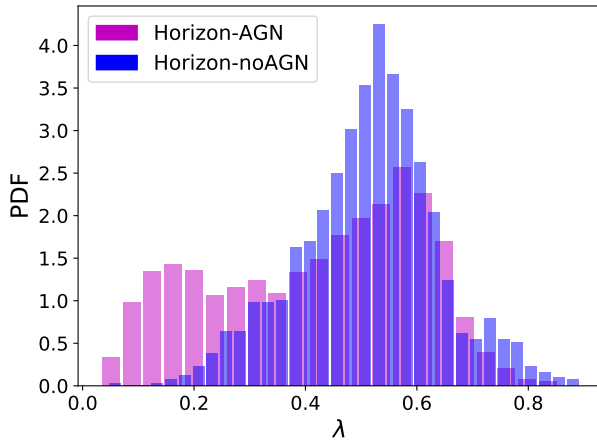


**Fig. 7.** Histograms of the spin parameter for ETGs from Horizon-AGN (magenta) and Horizon-noAGN (blue).

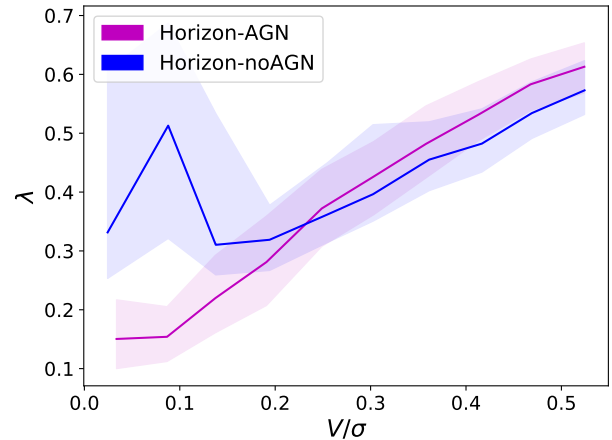


**Fig. 8.** Spin parameter as a function of  $V/\sigma$  for Horizon-AGN (magenta) and Horizon-noAGN (blue) samples. Shaded regions depict the 25 and 75 percentiles.

other parameters in this paper. The calculations are done by considering all stars within  $R_{\text{hm}}$ .

If we consider  $\lambda \sim 0.2$  as a suitable threshold to distinguish fast and slow rotators as in Rosito et al. (2019a), only 18 per-cent of the simulated ETGs are found to be slow rotators. In Fig. 7 we show a histogram of the spin parameters for these ETGs. For Horizon-AGN, we can observe a bimodality with peaks at  $\lambda \sim 0.1$  (slow rotators) and  $\lambda \sim 0.6$ . Graham et al. (2018) find a bimodality distribution of this parameter in observations, albeit the second peak is reported to be at  $\lambda \sim 0.9$ . The differences in the calculation of this parameter in that observational work must however be taken into account. We remark that in a previous work by Choi et al. (2018), where they use a relation between the spin parameter and the ellipticity to classify galaxies as slow/fast rotators, as in Emsellem et al. (2011), they find a fraction of 11.2 per-cent of slow rotators in Horizon-AGN. In their work they find a correlation of the amount of rotation with mass which is explained by the fact that massive galaxies have experienced a larger number of mergers regardless their environment and thus they rotate more slowly.

As expected, there is an even smaller fraction of slow rotators (defined above) in Horizon-noAGN (1 per-cent). This is consistent with the fact that in the absence of AGN, it is more difficult to reproduce massive ETGs (Dubois et al. 2016). For this simulation the distribution of  $\lambda$  is unimodal with a peak at about  $\lambda \sim 0.55$  (Fig. 7). Therefore, we can conclude that AGN feedback is important for reproducing the bimodality present in the observations (Graham et al. 2018) and hence, the angular momentum distribution of the stellar populations.

For the Horizon-AGN sample, the correlation between the spin parameter and  $V/\sigma$  is excellent (Fig. 8, magenta lines). For ETGs in Horizon-noAGN there is also a clear correlation when  $V/\sigma > 0.1$ . The high values of  $\lambda$  for galaxies with  $V/\sigma \leq 0.1$  in the Horizon-noAGN run are due to a small number of outliers. Therefore, the existence of the correlation between morphology and spin parameter is not affected. In fact, in Fig. 2 it can be appreciated that ETGs with these low  $V/\sigma$  have high inner disc fractions, which are consistent with the high  $\lambda$  parameters shown in Fig. 8.

## 5. The fundamental scaling relations and their redshift evolution

In this Section, we investigate the impact of the AGN feedback on the two fundamental relations: the mass–plane and the FP, their parameters compared to those obtained assuming virialization and their evolution with redshift.

### 5.1. The mass–plane

Let us first analyse the mass–plane for ETGs at different redshifts and how it evolves with time to assess when this relation started to be valid.

The mass–plane, which can be understood as a consequence of the virial theorem (Bolton et al. 2007), relates the dynamical mass with the galaxy radius,  $R$ , and the velocity dispersion,  $\sigma$  of galaxies:

$$M \propto \sigma^\alpha R^\beta / G. \quad (1)$$

According to the virial theorem, the exponents should be  $\alpha = 2$  and  $\beta = 1$  (see Binney & Tremaine 1987).

Instead of working with dynamical masses, we use stellar masses as in Oñorbe et al. (2005) and Oñorbe et al. (2006, see Introduction). We also estimate the velocity dispersion  $\sigma_e$  of the stellar populations computed within  $R_{\text{hm}}$ . In both Horizon simulations, we perform ordinary multiple linear regressions, being  $M_*$  the dependent variable, to obtain the parameters in Eq. (1) at each analysed redshift, as shown in Fig. 9. For comparison, we also include the virial relation ( $\alpha = 2$  and  $\beta = 1$ ) for  $z = 0$ . The constant term in that relation at  $z = 0$  is set *ad-hoc*. From this figure, we can appreciate that, in the presence of AGN, the mass–plane is in place since  $z = 3$  and is approximately consistent with the expectation from the virial theorem. On the other hand, the mass–plane for Horizon-noAGN ETGs is also in place since  $z = 3$ , but it is clearly more tilted from the virial relation. This indicates that, given the same conditions, AGN feedback is needed to regulate the SF allowing the fundamental relations to be built. All the parameters of the linear regression are summarized in Table 1. The fact that we find different parameters from the linear regressions for Horizon-noAGN indicates that AGN feedback affects not only the stellar mass, the size and the velocity dispersion but also the relation among them as as clearly

unveiled by the mass–plane. Even more, it regulates their evolution as a function of redshift yielding a weaker trend in agreement with observations, as we will discuss in more detail below.

For comparison with recent observations, we calculate the mass–plane for ETGs from ATLAS<sup>3D</sup> project (Cappellari et al. 2011) by ordinary multiple linear regressions. We adopted the stellar mass estimated by the JAM method which provides a more robust estimation which does not largely depend on the IMF (Cappellari et al. 2013b) and which better compares with the stellar mass estimated from the simulations. The effective radius (comparable with  $R_{\text{hm}}$ ) and the velocity dispersion within that radius are extracted from Cappellari et al. (2013a). The obtained parameters for Eq. (1) are  $\alpha_{\text{obs}} = 1.930 \pm 0.030$ ,  $\beta_{\text{obs}} = 0.925 \pm 0.020$  and  $C_{\text{obs}} = 6.241 \pm 0.064$ . We calculate the errors by a bootstrap method. Li et al. (2018) also calculate the mass–plane parameters for nearby elliptical and late-type galaxies (LTGs) classified by their Sérsic indexes (Sérsic 1968). They consider the major axis of the fitted ellipse of the half-light isophote, instead of the effective radius and twice the dynamical mass, instead of the stellar mass. By using least trimmed squares (LTS) regression (Rousseeuw & Leroy 1987), they obtain  $\alpha_{\text{obs}} = 1.959 \pm 0.018$  and  $\beta_{\text{obs}} = 0.964 \pm 0.013$  for the ETGs. Despite the fact that for both Horizon-AGN and Horizon-noAGN samples at  $z = 0$  the fitted parameters differ to those observed and to the theoretical values, the quantities  $\alpha$  and  $\beta$  computed for the former sample are in better agreement with observations than those computed for the latter, especially regarding  $\beta$ . At  $z = 0$  and  $z = 0.5$  the scatters of the linear regressions for Horizon-noAGN are notably lower than the others and this can explain the similarity between the magenta and blue curves in right panel of Fig. 9 and the 1:1 line (identity) besides the proximity of those curves to the observations albeit the mass–plane parameters calculated for that simulation at those redshifts are significantly different to the ones observed.

As can be appreciated from Table 2, the number of well-resolved ETGs decreases with increasing redshift. Moreover, there are less ETGs in the run without AGN feedback, as noted by Dubois et al. (2016). Nevertheless, the fraction of ETGs over the total number of galaxies with more than 5000 particles with  $R_{\text{hm}}$  greater than 2 kpc and those with realistic masses (see Sec. 3) remains approximately constant as a function of redshift in both simulations.

In order to evaluate the evolution of the mass–plane and to assess the effect of AGN feedback we use the parameters of Eq. (1) computed at  $z = 0$  (subscript  $z = 0$ ) to estimate the relation defined by Eq. (2) for ETGs from both simulations at different redshifts.

$$\log M_{\text{fit}} = \alpha_{z=0} \log \sigma_e + \beta_{z=0} \log R_{\text{hm}} + C_{z=0} \quad (2)$$

In Fig. 10 we show the difference between  $M_{\text{fit}}$  and the stellar mass measured at different redshifts as a function of the stellar mass. As can be seen, a systematic displacement towards higher positive differences are detected for galaxies from both simulations. From the inspection of this figure, when the AGN feedback is on, we note that there is no important evolution up to  $z = 1$ , when stellar masses are very close to  $M_{\text{fit}}$  in a wide range of masses and that the main difference is seen for  $1 < z < 3$  despite the fact that the mass–plane already exists since this redshift. As expected, at higher redshifts, stellar masses are lower. For Horizon-noAGN ETGs, there is a different scenario, in which evolution is more noticeable, but the displacement is still positive and increasing with redshift. From Table 1 we can see that

the scatter of the regression increases significantly, and the errors in the parameter  $\beta$  are extremely large at  $z = 2$  and  $z = 3$ . In fact,  $\beta$  is nearly zero for  $z = 2$  and, hence, there is almost no dependence on size in the mass–plane. For  $z = 3$  there is a small number of galaxies and the error for  $\beta$  is also very high. However the large value of the errors does not allow us to achieve robust conclusions with regards to these linear regressions.

## 5.2. The fundamental plane

The FP (Faber et al. 1987; Dressler et al. 1987; Djorgovski & Davis 1987) is an alternative representation of the fundamental relation depicted in the mass–plane, assuming homology and a constant  $M/L$  for all elliptical galaxies. Therefore, the functional form is similar:

$$R_{\text{eff}} \propto \sigma_e^\alpha I_e^\beta. \quad (3)$$

The subscript "e" indicates that the velocity dispersion is measured within  $R_{\text{eff}}$ , which is replaced with  $R_{\text{hm}}$  in the computation of simulated data. Here,  $I_e$  is the average surface brightness within the effective radius defined as  $I_e = L/(2\pi R_{\text{eff}}^2)$ . It is easy to see again that, assuming virialisation and homology,  $\alpha = 2$  and  $\beta = -1$  (e.g. Mo et al. 2010). There is, however, a tilt in the parameters which can be attributed to a variation of  $M/L$ , the dark matter fraction or possible non-universality of the IMF. It has been shown that a dynamical estimation of the stellar mass takes into account much of this tilt (Cappellari 2016). Since we are first interest in unveiling the role of AGN feedback on the FP, we work with stellar masses instead of luminosities (see Section 6 for a discussion on the latter).

We perform a similar analysis to that described in the last subsection. For each analysed redshift, we estimate the parameters in the Eq. (3) for ETGs with and without the action of AGN feedback by an ordinary multiple linear regression where the dependent variable now is  $R_{\text{hm}}$ . We replace  $I_e$  by  $\Sigma_e$  and thus the analysed FP is defined by the total stellar mass of the simulated galaxies. These stellar masses are comparable to the  $M_{\text{JAM}}$  estimated by Cappellari et al. (2013a). As regards the observations, by means of a multiple linear regression, we find the following values:  $\alpha_{\text{obs}} = 1.678 \pm 0.035$  and  $\beta_{\text{obs}} = -0.848 \pm 0.019$  where the errors are calculated with a bootstrap method.

From Fig. 11 it can be appreciated that the resultant planes are tight. This fact is explained by the low scatter in these regressions at all analysed redshifts, as shown in Table 3, where we include the parameters obtained for both Horizon simulations.

For the Horizon-AGN sample (left panel), the different FPs are tilted from the virial relation for galaxies at  $z = 0$  (see Table 3 and Fig. 11). This is consistent with many observational studies, as mentioned in the introduction. More specifically, the  $\beta$  parameter related with  $\Sigma_e$  is the most affected one at  $z = 0$ , while the  $\alpha$  parameter, related with  $\sigma_e$  is closer to the expected theoretical value. Regarding  $\beta$ , we note that  $|\beta| \leq |\beta_{\text{obs}}|$ . This can be related to the fact that  $M_{\text{JAM}}$  is a good approximation of the total stellar mass (Cappellari et al. 2013b), but there may be differences, especially due to variations in the IMF. Again, the zero-point of the virial relation was set *ad-hoc*.

On the other hand, the virial relation obtained from Horizon-noAGN galaxies at  $z = 0$  (right panel of Fig. 11) presents a remarkable break with respect to the slopes of the FP at all the redshifts considered in this paper. This means that, despite the fact that we can fit a plane at different redshifts with low scatter, in the absence of AGN feedback the observed relation cannot be reproduced, especially at radii larger than  $10^{0.6}$  kpc. It is clear

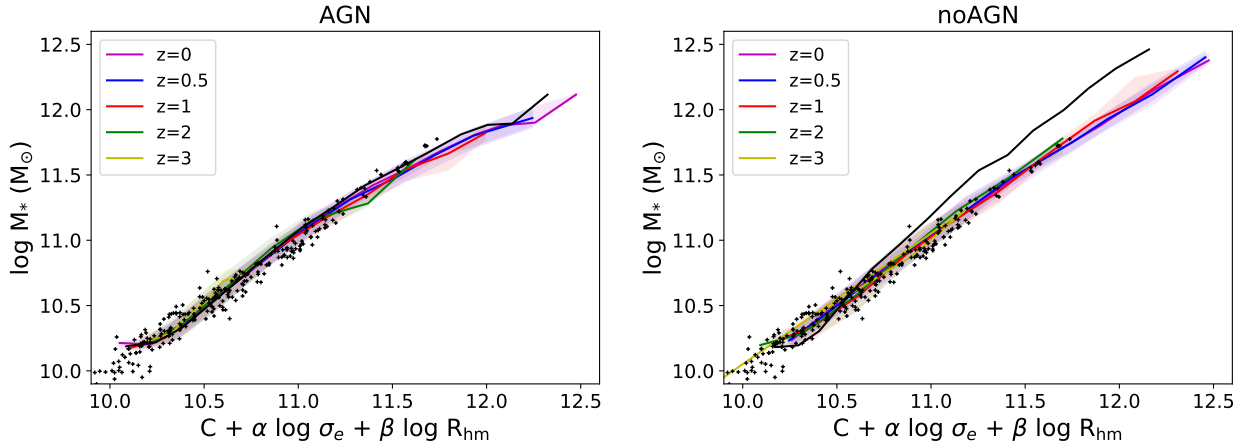


**Fig. 9.** Mass–plane as a function of redshift for ETGs from Horizon-AGN (left panel) and Horizon-noAGN (right panel). The magenta, blue, red, green and yellow lines depict the simulated relations at  $z = 0$ ,  $z = 0.5$ ,  $z = 1$ ,  $z = 2$  and  $z = 3$ , respectively. The shaded regions delimit the 25 and 75 percentiles. We also show the virial relation for  $z = 0$  in a black solid line. Observations from ATLAS<sup>3D</sup> project (Cappellari et al. 2011, 2013a,b) at  $z = 0$  are included for comparison (black crosses).

**Table 1.** Evolution of mass–plane parameters with and without AGN feedback. The parameters  $\alpha$  and  $\beta$  are given by Eq. (1). The errors are estimated by applying a bootstrap technique. The linear regression scatters are included ( $\sigma$ ).

| Redshift | Horizon-AGN       |                   |                   |          | Horizon-noAGN     |                    |                   |          |
|----------|-------------------|-------------------|-------------------|----------|-------------------|--------------------|-------------------|----------|
|          | $\alpha$          | $\beta$           | $C$               | $\sigma$ | $\alpha$          | $\beta$            | $C$               | $\sigma$ |
| 0        | $2.553 \pm 0.033$ | $0.710 \pm 0.017$ | $4.103 \pm 0.060$ | 0.103    | $2.898 \pm 0.013$ | $0.249 \pm 0.028$  | $3.563 \pm 0.032$ | 0.066    |
| 0.5      | $2.333 \pm 0.030$ | $0.794 \pm 0.024$ | $4.559 \pm 0.054$ | 0.099    | $2.725 \pm 0.023$ | $0.151 \pm 0.055$  | $4.093 \pm 0.036$ | 0.079    |
| 1        | $2.190 \pm 0.031$ | $0.945 \pm 0.027$ | $4.734 \pm 0.057$ | 0.097    | $2.665 \pm 0.036$ | $0.233 \pm 0.103$  | $4.098 \pm 0.062$ | 0.108    |
| 2        | $2.032 \pm 0.044$ | $0.722 \pm 0.040$ | $5.253 \pm 0.087$ | 0.115    | $2.460 \pm 0.061$ | $-0.021 \pm 0.134$ | $4.628 \pm 0.123$ | 0.133    |
| 3        | $1.573 \pm 0.088$ | $0.668 \pm 0.078$ | $6.266 \pm 0.207$ | 0.117    | $2.418 \pm 0.167$ | $0.706 \pm 0.647$  | $4.248 \pm 0.492$ | 0.186    |

**Table 2.** Well-resolved ETGs the Horizon simulations at different redshifts.

| z   | Number      |               | Fraction over total number |               |
|-----|-------------|---------------|----------------------------|---------------|
|     | Horizon-AGN | Horizon-noAGN | Horizon-AGN                | Horizon-noAGN |
| 0   | 4370        | 1560          | 0.25                       | 0.08          |
| 0.5 | 3641        | 745           | 0.23                       | 0.04          |
| 1   | 3034        | 441           | 0.24                       | 0.03          |
| 2   | 1507        | 274           | 0.26                       | 0.03          |
| 3   | 372         | 39            | 0.32                       | 0.04          |

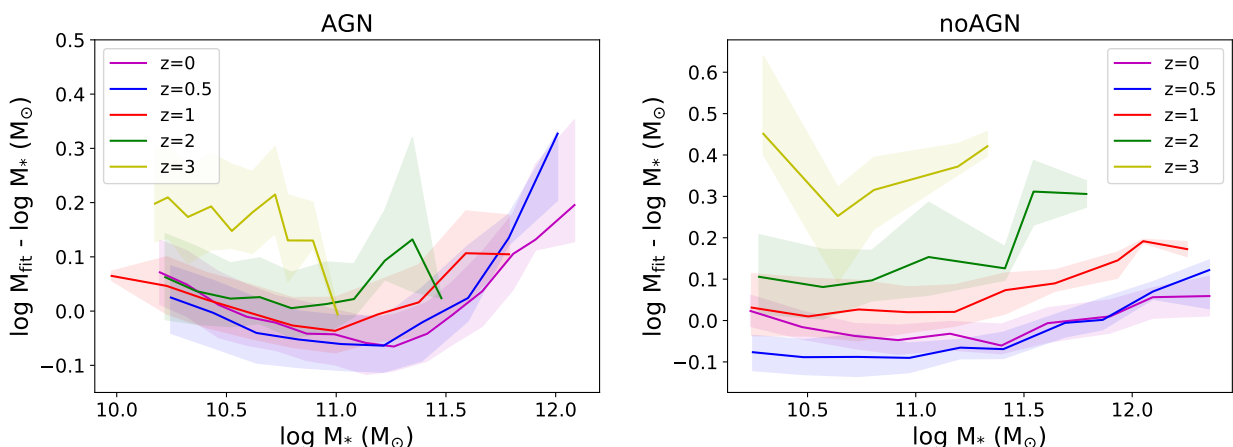


**Fig. 10.** Differences between  $\log M_{\text{fit}}$  (defined in Eq. 2) computed with parameters at  $z = 0$  and stellar mass at different redshifts for ETGs from Horizon-AGN (left panel) and Horizon-noAGN (right panel). The magenta, blue, red, green and yellow lines depict the simulated relations at  $z = 0$ ,  $z = 0.5$ ,  $z = 1$ ,  $z = 2$  and  $z = 3$ , respectively. The shaded regions delimit the 25 and 75 percentiles.

that without the regulation of the stellar mass and size by AGN feedback, the FP plane departures largely from the expectation of the virial theorem.

We follow the approach of Rosito et al. (2018) and Rosito et al. (2019b), and use the observed parameters of the FP obtained using the  $M_{\text{JAM}}$  to compute  $\Sigma_e$  (Cappellari et al. 2013a). We use the observed slopes at  $z = 0$ , to estimate the FP as defined in Eq. (4), at the analysed redshifts. The constant term is set *ad-hoc*.

$$\text{FP} = \alpha_{\text{obs}} \log \sigma_e + \beta_{\text{obs}} \log \Sigma_e + C \quad (4)$$

Hence we obtained the  $R_{\text{hm}}$  which should be measured in case the relation does not evolve. These values are compared to the measured  $R_{\text{hm}}$ . The results are shown in Fig. 12. From this figure, we can see a consistency of the simulated FP for the Horizon-AGN sample with these parameters. However, in the absence of AGN feedback, the FP departs from the observed relation at high radii. This break from the FP in the Horizon-noAGN ETGs is produced by an excess of stellar mass at given  $R_{\text{hm}}$ , which produces the excessive  $\Sigma_e$  as previously mentioned. To illustrate this, in Fig. 13 we show the relation for  $z = 0$  together with the individual simulated galaxies. It can be appreciated that the deviation from the observed FP at large radii in Horizon-noAGN is caused by galaxies with high average surface density ( $\Sigma_e > 10^{9.5} \text{ M}_\odot \text{ kpc}^{-2}$ ) at a given  $R_{\text{hm}}$  (right panel). Hence AGN feedback plays an important role in regulating the SF and prevents the formation of very dense galaxies, which otherwise depart from the FP. This trend is in agreement with Peirani et al. (2019) who already reported higher values of  $\Sigma_e$  for galaxies formed in absence of AGN in the Horizon simulation. These galaxies clearly do not follow the FP however they are still consistent with the mass–plane. For comparison, we include the scatter plot for Horizon-AGN at  $z = 0$ , where we do not find such dense galaxies.

## 6. Discussion on the FP

In the previous section, we have shown the impact of AGN feedback on ETGs allows their FP to be reproduced. Here we explore in more detail the correlation between different galaxy properties and the FP as a function of redshift with the aim at discovering how AGN feedback works at different mass scales and redshifts.

### 6.1. sSFR, age and morphology dependence

One of the main roles of AGN feedback is the regulation of the SF activity. This can be clearly appreciated from Fig. 14 where the median sSFR as a function of the stellar mass for the different analysed redshifts are shown. For the noAGN run, the sSFR decreases with decreasing redshift as expected, however it remains approximately constant as a function of stellar mass (right panel). The activation of the AGN feedback modulates the SF activity across time with the larger impact at about  $z = 1$  where it is quenched principally for high mass galaxies (see also Beckmann et al. 2017). The overall effect is a change in the slope of this relation, which better reproduces the observed trend, although they have still more SF activity than observed (see Fig. 4).

The quenching of the SF activity is reflected on the evolution of mean ages of the stellar populations. In Fig. 15 we show the FP for both simulations as a function of mass-weighted av-

erage stellar age<sup>4</sup>. At  $z = 0$ , galaxies dominated by old stars lie above the 1:1 line, especially for large radii. The opposite trend can be observed for higher redshifts ( $z = 2$  and  $z = 3$ ), while the transition between these behaviours occurs at about  $z = 1$ . In Fig. 14 (left panel), it can be noticed that, at that redshift, there is a change in the slope of the sSFR as a function of stellar mass. For  $z \leq 1$  the action of AGN feedback is stronger for more massive ETGs, since the negative slope in the relation between sSFR and stellar mass is steeper while for the noAGN run the regulation of SF is insufficient to build the old dominant stellar population in galaxies located above the 1:1 line.

The change with redshift in the distribution of ages across the FP is also correlated with the trend observed for the  $V/\sigma$  parameter across that plane as can be seen from Fig 16 (left panels). This shows a link between star formation histories and galaxy morphologies (quantified by  $V/\sigma$ , see Fig B.2). Those galaxies which are faster rotators tend to have younger stellar populations, on average. At  $z = 1$ , galaxies dominated by velocity dispersion present larger sizes compared to those more rotation dominated. Those with  $V/\sigma$  within the range [0.30-0.35] depict a U-shape in the distribution across the FP at a given galaxy size. In the absence of AGN feedback, galaxies dominated by velocity dispersion are systematically located above the 1:1 relation. The redshift evolution of the age distribution reflects the fact that for  $z > 1$  the insufficient regulation of SF prevents the formation of big ETGs dominated by old stellar populations.

Chisari et al. (2018) study the power spectrum from different Horizon simulations to assess the impact of the modelling of baryonic physics and AGN feedback in the distribution of matter. By analysing the power spectrum at different cosmic times they found that at  $z \geq 1$  AGN decreases the power, and that suppression increases with decreasing redshift for all scales because of the black holes that continue to grow at those times. At small scales ( $k \geq 10 \text{ h/Mpc}$ ) this suppression is more notable. This can be related to the results in Beckmann et al. (2017), where they link the AGN feedback with the quenching of SF in the sense that, on small scales AGN heats the gas and prevents SF, thus regulating the baryonic matter content. There is an important change at  $z = 1$  (the same time considered above): at intermediate scales ( $k \sim 2 \text{ h/Mpc}$ ) the impact of the AGN in the power spectrum is reduced because of the decrease in the efficiency of black hole accretion (Volonteri et al. 2016) and subsequent decrease in feedback energy. Peirani et al. (2017) also note this decrease that involves lower values of  $\chi$  (see Section 2) implies a transition to the radio mode dominated feedback. Furthermore, by comparing their results with other simulations, Chisari et al. (2018) conclude the need of modelling a stronger AGN feedback in agreement with our findings.

### 6.2. The mass-to-light ratio variation across the FP

Hereafter we will focus on the AGN run, which better reproduces the observations. The regulation of the SF activity by AGN feedback also modulates the luminosities and, consequently, the  $M/L$ <sup>5</sup>. As can be seen from Fig. 17 the FP as a function of  $M/L$  in the  $r$ -band shows a clear change from a sequence of galaxies

<sup>4</sup> Hereafter, in plots depicting two variables as a function of a third one, we fix the colour-bar limits to the first and third quartiles of the corresponding values according to which the symbols are coloured.

<sup>5</sup> Simulated AB magnitudes are obtained by means of SP models from Bruzual & Charlot (2003) and a Salpeter IMF. The total flux for each frequency is passed through the different SDSS filters, in particular the  $r$ -band. See more details in Chisari et al. (2015)

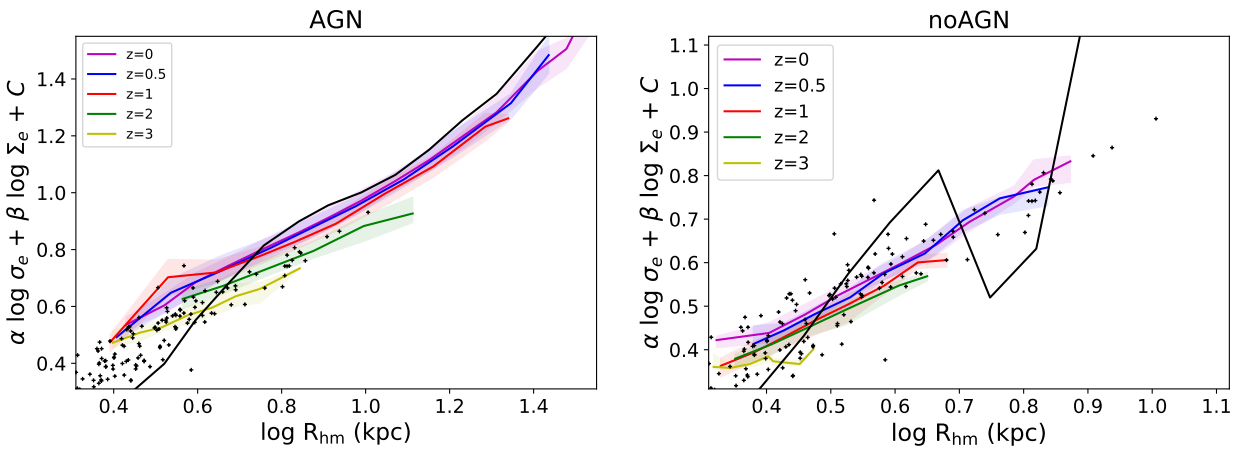


**Fig. 11.** The FP as a function of redshift for ETGs from Horizon-AGN (left panel) and Horizon-noAGN (right panel). The magenta, blue, red, green and yellow lines depict the simulated relations at  $z = 0$ ,  $z = 0.5$ ,  $z = 1$ ,  $z = 2$  and  $z = 3$ , respectively. The regions between the 25 and 75 percentiles are shaded. We include the virial relation for galaxies at  $z = 0$  (black solid line). For comparison, we also include observational results from ATLAS<sup>3D</sup> in black crosses.

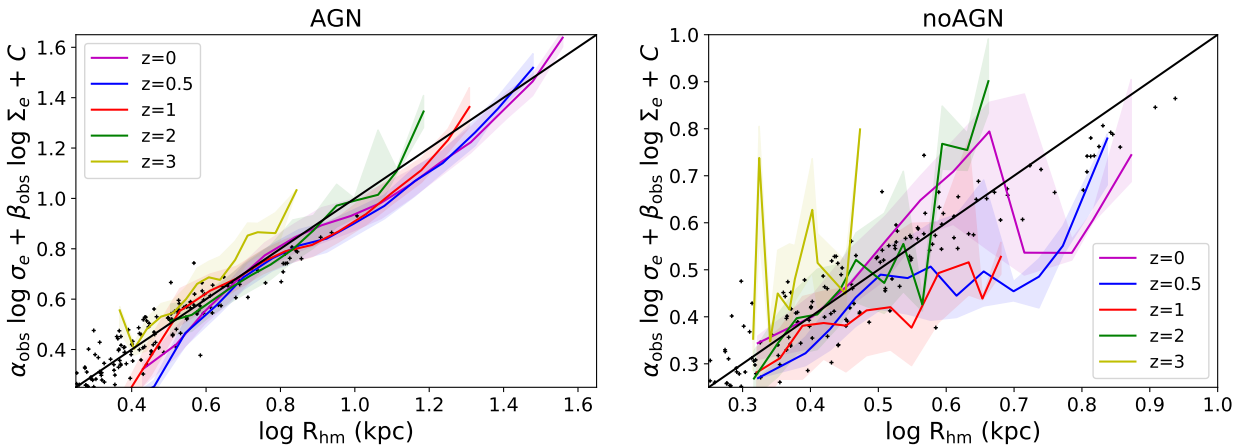


**Fig. 12.** The FP for Horizon-AGN (left panel) and Horizon-noAGN (right panel) galaxies obtained with the parameters calculated with data from Cappellari et al. (2013a) estimated at  $z = 0$  (magenta lines),  $z = 0.5$  (blue lines),  $z = 1$  (red lines),  $z = 2$  (green lines) and  $z = 3$  (yellow lines). The regions between the 25 and 75 percentiles are shaded. For comparison, we also include the observational results from ATLAS<sup>3D</sup> (black crosses). The 1:1 line is depicted in black.

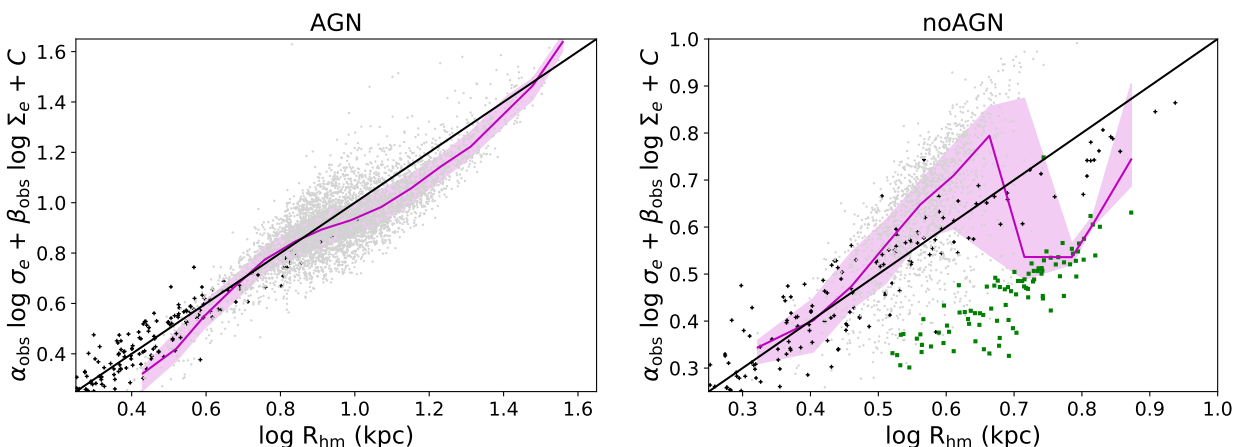


**Fig. 13.** The FP for Horizon-AGN ETGs (left panel) and for Horizon-noAGN galaxies (right panel) computed with the parameters obtained with data from Cappellari et al. (2013a) including its scatter plot (gray dots) at  $z = 0$ . Magenta lines and the shaded region are as in Fig. 12. Galaxies with average surface density greater than  $10^{9.5} M_{\odot} \text{ kpc}^{-2}$  are depicted (green squares). There are not such dense galaxies in Horizon-AGN sample. We include observations from ATLAS<sup>3D</sup> for comparison (black crosses). The 1:1 line is depicted in black.

**Table 3.** Evolution of FP parameters in Horizon simulations using  $\Sigma_e$ . The parameters  $\alpha$  and  $\beta$  are given by Eq.(3). The errors are estimated by applying a bootstrap technique. The linear regression scatter is included ( $\sigma$ ).

| Redshift | Horizon-AGN       |                    |                   |          | Horizon-noAGN     |                    |                   |          |
|----------|-------------------|--------------------|-------------------|----------|-------------------|--------------------|-------------------|----------|
|          | $\alpha$          | $\beta$            | $C$               | $\sigma$ | $\alpha$          | $\beta$            | $C$               | $\sigma$ |
| 0        | $1.700 \pm 0.017$ | $-0.542 \pm 0.007$ | $1.345 \pm 0.040$ | 0.066    | $1.317 \pm 0.027$ | $-0.440 \pm 0.010$ | $1.251 \pm 0.027$ | 0.033    |
| 0.5      | $1.471 \pm 0.017$ | $-0.475 \pm 0.009$ | $1.331 \pm 0.047$ | 0.062    | $1.069 \pm 0.030$ | $-0.355 \pm 0.014$ | $1.101 \pm 0.051$ | 0.035    |
| 1        | $1.360 \pm 0.024$ | $-0.468 \pm 0.012$ | $1.490 \pm 0.057$ | 0.064    | $0.921 \pm 0.041$ | $-0.299 \pm 0.017$ | $0.884 \pm 0.060$ | 0.045    |
| 2        | $0.990 \pm 0.033$ | $-0.375 \pm 0.013$ | $1.503 \pm 0.068$ | 0.062    | $0.726 \pm 0.051$ | $-0.261 \pm 0.022$ | $0.999 \pm 0.104$ | 0.048    |
| 3        | $0.695 \pm 0.051$ | $-0.366 \pm 0.020$ | $2.001 \pm 0.152$ | 0.061    | $0.168 \pm 0.134$ | $-0.084 \pm 0.050$ | $0.714 \pm 0.192$ | 0.047    |

**Table 4.** Evolution of L-FP parameters in presence of AGN feedback for all ETGs and for the subsample obtained with the restriction  $V/\sigma < 0.3$ . The parameters  $\alpha_I$  and  $\beta_I$  are given by Eq.(3). The errors are estimated by applying a bootstrap technique. The linear regression scatter is included ( $\sigma$ ).

| Redshift | Whole sample      |                    |                   |          | Restriction to $V/\sigma < 0.3$ |                    |                   |          |
|----------|-------------------|--------------------|-------------------|----------|---------------------------------|--------------------|-------------------|----------|
|          | $\alpha_I$        | $\beta_I$          | $C_I$             | $\sigma$ | $\alpha_I$                      | $\beta_I$          | $C_I$             | $\sigma$ |
| 0        | $1.388 \pm 0.013$ | $-0.379 \pm 0.004$ | $0.605 \pm 0.033$ | 0.067    | $1.313 \pm 0.018$               | $-0.363 \pm 0.008$ | $0.658 \pm 0.048$ | 0.067    |
| 0.5      | $1.181 \pm 0.011$ | $-0.324 \pm 0.006$ | $0.720 \pm 0.037$ | 0.063    | $1.194 \pm 0.016$               | $-0.321 \pm 0.008$ | $0.666 \pm 0.056$ | 0.063    |
| 1        | $1.108 \pm 0.015$ | $-0.341 \pm 0.007$ | $1.037 \pm 0.047$ | 0.062    | $1.188 \pm 0.021$               | $-0.372 \pm 0.011$ | $1.098 \pm 0.069$ | 0.065    |
| 2        | $1.028 \pm 0.028$ | $-0.412 \pm 0.013$ | $1.813 \pm 0.072$ | 0.056    | $1.100 \pm 0.042$               | $-0.420 \pm 0.019$ | $1.710 \pm 0.106$ | 0.055    |
| 3        | $0.796 \pm 0.056$ | $-0.373 \pm 0.018$ | $1.981 \pm 0.140$ | 0.053    | $0.804 \pm 0.103$               | $-0.381 \pm 0.036$ | $2.036 \pm 0.246$ | 0.059    |

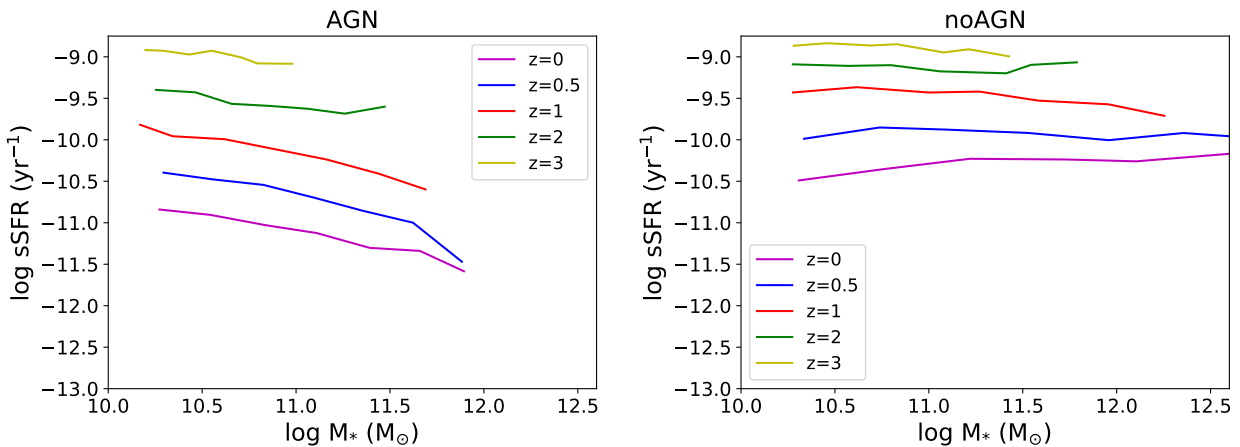


**Fig. 14.** sSFR as a function of stellar mass for Horizon-AGN (left panel) and Horizon-noAGN (right panel) at different redshifts. At  $z = 1$  there is a change in the slope for the Horizon-AGN samples while in absence of AGN feedback, the sSFR does not depend on stellar mass.

dominated by young stars with lower  $M/L$  which are more dominated by rotation to populate the region above the 1:1 relation for  $z > 1$  whereas the opposite is detected for those with older stellar populations. As previously stated, at  $z \sim 1$  the action of AGN feedback can be linked to a quenching of the SF and the progressive aging of the stellar populations. The evolution with  $M/L$  can be traced in the stellar aging evolution.

The comparison with observations is more direct if average surface brightness is used to construct the FP (L-FP, hereafter subscript I). It is also well-known that in this case, a significant tilt of the L-FP is expected. In order to estimate the L-FP we used the luminosities in  $r$ -band.

In Fig. 18, we display the L-FP as a function of redshift for the Horizon-AGN. For comparison the expected relation from the virial theorem is included. As can be seen, the tilt is strong at all redshifts (Table 4) whereas when using the stellar mass, the deviation from the virial expectations are weaker for  $z = 0$  (Fig. 11). Our results show that an important factor causing the tilt in the L-FP is produced by the variation of the  $M/L$  from galaxy to galaxy and as a function of redshift which have been shown in Fig. 17.

In summary, the action of AGN feedback in the Horizon simulations regulates the SF activity so that it is significantly quenched by  $z = 1$  and mainly for more massive galaxies. This also has an impact on the  $M/L$  ratios which get larger with decreasing redshift as the stellar populations age (Fig. 17). However, this is not the only effect. Some galaxies have lower  $\Sigma_e$  at similar  $M/L$ , as shown in Fig. 19. Additionally, we also find that  $V/\sigma$  varies, so that more massive spheroidal-dominated galaxies are able to form. In Fig. 19 we can see clearly how the AGN feedback changes the  $M/L$  ratio for galaxies of intermediate and large  $\sigma_e$ .

In a recent observational work, Bernardi et al. (2020) analyse the FP of nearby galaxies from MaNGA DR15 (Aguado et al. 2019). They found a tight plane, especially for slow rotator ETGs. In agreement with Saglia et al. (1993), who found a dependence of the FP on morphology, Bernardi et al. (2020) remark that the FP parameters are linked to the morphological mix of ETGs. Our results are in global agreement with this trend at  $z = 0$  although the simulated L-FP is more tilted for the coefficient of the surface brightness compared to Bernardi et al. (2020) ( $\alpha_{\text{obs}} = 1.275 \pm 0.025$  and  $\beta_{\text{obs}} = -0.723 \pm 0.013$ ). Their L-FP

is also tight with a similar value for the scatter (0.077) similar to the Horizon-AGN (0.067).

Lu et al. (2020) studied the evolution of the FP from the IllustrisTNG-100 simulation, finding that the plane exists and is tight since  $z = 2$ , in agreement with our findings. There are, however, differences in the fitted parameters comparing their Table 1 and our Table 4 regarding the whole sample. Our  $\alpha_I$  parameters are slightly different to theirs taking into account the errors at all redshifts with exception of  $z = 2$  in which both calculations are consistent. On the other hand,  $\beta_I$  values are always more negative than those reported by Lu et al. (2020). In both works, parameters evolve with time with similar scatter. These authors report an increase of the dispersion with older stellar ages.

In order to better compare our results with those of Lu et al. (2020), we must take into account that their galaxy sample was selected by adopting different criteria. If we restrict our sample to the most dispersion-dominated galaxies by imposing  $V/\sigma < 0.3$ , then the dependency on stellar age is more consistent with Lu et al. (2020) at  $z = 0$  as many of the faster rotator ETGs in Horizon-AGN are excluded. Moreover,  $\alpha_I$  parameters in Table 4 are consistent to those reported by Lu et al. (2020) within the errors. As it can be seen from Fig. 20, the age dependency is similar at all analysed redshifts, with galaxies dominated by old stars having more positive residuals (defined by  $\text{Res} = \alpha_I \log \sigma_e + \beta_I \log I_e + C - \log R_{\text{hm}}$  where the coefficients are computed at each redshift). However, we find that galaxies with similar mean ages are located on planes which are tilted respect to the overall L-FP. In Fig. 20 the L-FP restricted to slower rotators ETGs shows a similar trend with age to that reported by Lu et al. (2020). These trends are different from what we found for the stellar mass FP where for  $z > 1$  galaxies with young stellar populations tend to have positive residual (with an analogous definition) while at  $z = 1$  there is an inversion in the relation which drives the final age distribution at  $z = 0$ . The variation of stellar age across the FP is related to the  $M/L$  for galaxies with different  $\Sigma_e$ . From Fig. 19 we can see that high  $\Sigma_e$  galaxies have high  $\sigma_e$  and low  $M/L$  at high redshift, but at a given  $\sigma_e$  some galaxies become denser as the  $M/L$  get higher for lower redshift. For  $z < 1$  the dependence on  $\Sigma_e$  has changed slope with some galaxies becoming less dense for a given  $\sigma_e$  and  $M/L$ .

In Fig. 21 we show the residuals of the L-FP at  $z = 0$  for the ETGs sample with the restriction  $V/\sigma < 0.3$  (black line and gray shaded regions). Additionally, we also show the residuals considering an extra condition to select only passive galaxies according to Lacerna et al. (2014). Consequently, only those ETGs that satisfies this conditions:  $\log(\text{sSFR}) \leq -0.65(\log(M_*) - 10) - 10.85$  ( $M_*$  is in units of  $h^{-2} M_\odot$  and sSFR is in units of  $\text{yr}^{-1}$ ) as a function of stellar age. As can be seen from Fig. 21, we remark the qualitative similarity in the trend obtained for passive galaxies in Horizon-AGN with the results presented by Lu et al. (2020) since both sets of residuals depict an monotonous increasing function of stellar age<sup>6</sup>. The plot is consistent with Fig. 20 taking into account the range of ages. However, ETGs with  $V/\sigma < 0.3$  dominated by younger stars present a different behaviour. If we take into account the whole age range,  $[10^{9.51} - 10^{10.04}] \text{ yr}$ , there is a small number of galaxies with positive residuals. In particular, there are 22 ETGs (defined with the restriction  $V/\sigma < 0.3$ ) with ages lower than  $10^{9.75} \text{ yr}$ , 14 of them with positive residuals. These slow rotators ETGs have been rejuvenated and hence determined a turn in the residual relation. These younger galaxies represent 1.11 per-cent of the restricted ETGs sample at  $z = 0$ . Besides, younger galaxies with positive

residuals represent 0.70 per-cent of this sample. These fractions increase to 3.23 and 1.72 per-cent when the constrain on  $V/\sigma$  is relaxed. The confrontation of these results with recent reported observation of ETGs by Lacerna et al. (2020) could shade light on the efficiency of feedback mechanisms.

## 7. Conclusions

We have performed a comprehensive study of ETGs from both, Horizon-AGN and Horizon-noAGN simulations, which allow us to analyse the role of AGN feedback in reproducing the main scaling relations for this type of galaxies. We select objects resolved with more than 5000 stellar particles,  $R_{\text{hm}}$  higher than 2 kpc and total stellar masses lower than  $10^{12.5} M_\odot$ . Galaxies are classified as ETGs following the morphological classification in Chisari et al. (2015) by using  $V/\sigma < 0.55$ .

Our main conclusions are:

- ETGs albeit dispersion-dominated by definition show a variety of morphologies, ranging from less to more rotational supported systems. They show a rotational component within their inner region (defined in Sec. 3.2). The stellar mass fraction of this rotational component to the dispersion-dominated component correlates with  $V/\sigma$  for ETGs in Horizon-AGN in agreement with previous results (Rosito et al. 2018, 2019b). ETGs in Horizon-noAGN show higher fractions which are independent of stellar mass. This implies that ETGs are more dominated by rotation in the Horizon-noAGN and that AGN feedback contributes to build up more dispersion-dominated systems leading to a better agreement with observations.
- The presence of AGN feedback is required to reproduce the bimodality in the spin parameter found in Graham et al. (2018). This clearly suggests that AGN feedback has an impact on the angular momentum retained by ETGs consistent with the previous item.
- At  $z = 0$  ETGs in Horizon-AGN are more quenched than those in Horizon no-AGN. The former show a decreasing trend with stellar mass in agreement with observations however, they are still more active than expected.
- In both simulations, there is a tight relation between mass and radius. Horizon-AGN galaxies present clearer trends of rotation and age (more massive galaxies are older and slower rotators) across the mass-size relation than those found in the absence of AGN. Moreover, a non-negligible old population in low-mass galaxies is found in Horizon-noAGN, which may be attributed to the fact that these systems are more affected by SN feedback added to the lack of calibration of this kind of feedback in this simulation. The mass-size relation for Horizon-AGN yields that larger mass galaxies have older stellar populations and are slower rotators. The transition to ETGs dominated by younger stars and more rotationally supported occurs at about 6 kpc. Around this radius, the mean stellar mass is  $\sim 1.4 \times 10^{12} M_\odot$  and the mean dynamical mass is  $\sim 1.5 \times 10^{12} M_\odot$ .
- In Horizon-AGN, we find evolution of the mass–plane for  $z < 1$ , which gets stronger for  $z > 1$ . This is in line with the redshift at which AGN feedback starts to have an impact in the steeper slope of the relation between sSFR and stellar mass. In Horizon-noAGN, the mass–plane evolves strongly for  $z > 0$ . The tilt from the virial relation is more important in the absence of AGN feedback. In the Horizon-AGN simulation, the coefficient of velocity dispersion remains closer to that expected from the virial theorem as a function of redshift, whereas the coefficient of  $R_{\text{hm}}$  is slightly smaller than the theoretical one.

<sup>6</sup> We utilised the moving median to estimate this relation

- The FP of ETGs with AGN follows a similar relation to that observed at  $z = 0$  (Cappellari et al. 2013a), unlike the FP without AGN. In particular, the main difference is caused by extended galaxies with high surface density, which was previously noticed by Peirani et al. (2019). This suggests the importance of this process in this relation. The evolution of the FP with redshift in Horizon-AGN is not clear whereas, in Horizon-noAGN the results are very different for radii larger than  $\sim 4$  kpc at different epochs.
- The SF activity is regulated by AGN feedback so that the observed anti-correlation between the sSFR and the stellar mass are reproduced. However, we notice that such regulation is not enough to reproduce Hernández-Toledo et al. (2010) and Gavazzi et al. (2003) lower values of sSFR. We note that there are recent observations of more star forming galaxies (Yates & Kauffmann 2014; Lacerna et al. 2020) which should be taken into account when revising the models. Horizon-noAGN ETGs present an excess of sSFR with similar values for all analysed stellar masses. The evolution of the sSFR as function of time shows a similar flat trend contrary to the relations obtained when AGN feedback is turned on. Hence, AGN feedback is not only regulating the level of star formation activity as a function of redshift but it is also modulating it as a function of stellar mass in order to produce the observed relations as expected.
- The action of AGN feedback that regulates the SF activity also has an impact on the  $M/L$  ratios which get larger with decreasing redshift as the stellar population ages. The variation of the  $M/L$  as a function of stellar mass surface density explains the differences found in L-FP which is strongly tilted with respect to the theoretical prediction compared to the weaker one found when using surface stellar density.
- When restricting to passive galaxies our ETGs, we found that those with positive residuals in the L-FP plane are dominated by older stellar populations and the residuals increase for increasing age in agreement with Lu et al. (2020) for the IllustrisTNG simulation. There is 0.70 per-cent of ETGs with  $V/\sigma < 0.3$  which have been slightly rejuvenated and have positive residuals.

Overall, our findings show that in order to reproduce the level of rotation, the sSFR- $M_*$  and the fundamental relations, AGN feedback is required principally at the massive end. We find that the FP is more sensitive to the action of the AGN feedback since it affects the stellar surface density and the  $M/L$  significantly. The evolution of the FP as well as its dependence on stellar age and galaxy morphology can thus provide detailed insight into the action of AGN feedback as a function of time.

**Acknowledgements.** PBT acknowledges support from CONICYT project Basal AFB-170002 (Chile) and Fondecyt Regular 1200703-2020. This work was partially supported through MINECO/FEDER (Spain) PGC2018- 094975-C21 grant. This project has received funding from the European Union's Horizon 2020 Research and Innovation Programme under the Marie Skłodowska-Curie grant agreement No 734374- LACEGAL. MSR and PBT acknowledge funding from the same Horizon 2020 grant for a seconddment at the Astrophysics group of Univ. Autónoma de Madrid (Madrid, Spain). This work has made use of the HPC resources of CINES (Jade and Occigen supercomputer) under the time allocations 2013047012, 2014047012 and 2015047012 made by GENCI. This work is partially supported by the Spin(e) grants ANR-13-BS05-0005 (<http://cosmicorigin.org>) of the French Agence Nationale de la Recherche and by the ILP LABEX (under reference ANR-10-LABX-63 and ANR-11-IDEX-0004-02). We thank S. Roubertol for running smoothly the Horizon cluster for us. Part of the analysis of the simulation was performed on the DiRAC facility jointly funded by STFC, BIS and the University of Oxford. This work is part of the Delta ITP consortium, a program of the Netherlands Organisation for Scientific Research (NWO) that is funded by the Dutch Ministry of Education, Culture and Science (OCW). NEC was partly supported by a Royal Astronomical Society Research fellowship during the preparation of this work.

## References

Aguado, D. S., Ahumada, R., Almeida, A., et al. 2019, ApJS, 240, 23

Argudo-Fernández, M., Lacerna, I., & Duarte Puetas, S. 2018, A&A, 620, A113

Aubert, D., Pichon, C., & Colombi, S. 2004, MNRAS, 352, 376

Avila-Reese, V., Zavala, J., & Lacerna, I. 2014, MNRAS, 441, 417

Baldry, I. K., Glazebrook, K., Brinkmann, J., et al. 2004, ApJ, 600, 681

Beckmann, R. S., Devriendt, J., Slyz, A., et al. 2017, MNRAS, 472, 949

Bernardi, M., Domínguez Sánchez, H., Margalef-Bentabol, B., Nikakhtar, F., & Sheth, R. K. 2020, MNRAS, 494, 5148

Bernardi, M., Sheth, R. K., Annis, J., et al. 2003, AJ, 125, 1866

Bertin, G., Ciotti, L., & Del Principe, M. 2002, A&A, 386, 149

Binney, J. & Tremaine, S. 1987, Galactic dynamics

Bolton, A. S., Burles, S., Treu, T., Koopmans, L. V. E., & Moustakas, L. A. 2007, ApJ, 665, L105

Borriello, A., Salucci, P., & Danese, L. 2003, MNRAS, 341, 1109

Bruzual, G. & Charlot, S. 2003, MNRAS, 344, 1000

Bryant, J. J., Owers, M. S., Robotham, A. S. G., et al. 2015, MNRAS, 447, 2857

Burkert, A. 2004, in Astronomical Society of the Pacific Conference Series, Vol. 322, The Formation and Evolution of Massive Young Star Clusters, ed. H. J. G. L. M. Lamers, L. J. Smith, & A. Nota, 489

Cappellari, M. 2016, ARA&A, 54, 597

Cappellari, M., Emsellem, E., Krajnović, D., et al. 2011, MNRAS, 413, 813

Cappellari, M., McDermid, R., Alatalo, K., et al. 2013a, MNRAS, 432, 1709

Cappellari, M., McDermid, R. M., Alatalo, K., et al. 2013b, MNRAS, 432, 1862

Chisari, N., Codis, S., Laigle, C., et al. 2015, MNRAS, 454, 2736

Chisari, N. E., Richardson, M. L. A., Devriendt, J., et al. 2018, MNRAS, 480, 3962

Choi, H., Yi, S. K., Dubois, Y., et al. 2018, ApJ, 856, 114

Ciotti, L., Lanzoni, B., & Renzini, A. 1996, MNRAS, 282, 1

Clauwens, B., Schaye, J., Franx, M., & Bower, R. G. 2018, MNRAS, 478, 3994

Cleveland, W. S. & Devlin, S. J. 1988, Journal of the American Statistical Association, 83, 596

Cook, M., Lapi, A., & Granato, G. L. 2009, MNRAS, 397, 534

Crain, R. A., Schaye, J., Bower, R. G., et al. 2015, MNRAS, 450, 1937

Croom, S. M., Lawrence, J. S., Bland-Hawthorn, J., et al. 2012, MNRAS, 421, 872

Dekel, A. & Silk, J. 1986, ApJ, 303, 39

Djorgovski, S. & Davis, M. 1987, ApJ, 313, 59

Domínguez-Tenreiro, R., Oñorbe, J., Martínez-Serrano, F., & Serna, A. 2011, MNRAS, 413, 3022

Domínguez-Tenreiro, R., Oñorbe, J., Sáiz, A., Artal, H., & Serna, A. 2006, ApJ, 636, L77

Dressler, A., Lynden-Bell, D., Burstein, D., et al. 1987, ApJ, 313, 42

Dubois, Y., Devriendt, J., Slyz, A., & Teyssier, R. 2012, Monthly Notices of the Royal Astronomical Society, 420, 2662

Dubois, Y., Gavazzi, R., Peirani, S., & Silk, J. 2013, MNRAS, 433, 3297

Dubois, Y., Peirani, S., Pichon, C., et al. 2016, MNRAS, 463, 3948

Dubois, Y., Pichon, C., Welker, C., et al. 2014, MNRAS, 444, 1453

Dubois, Y. & Teyssier, R. 2008, A&A, 477, 79

Dutton, A. A. & Treu, T. 2014, MNRAS, 438, 3594

Emsellem, E., Cappellari, M., Krajnović, D., et al. 2011, MNRAS, 414, 888

Faber, S. M., Dressler, A., Davies, R. L., Burstein, D., & Lynden-Bell, D. 1987, in Nearly Normal Galaxies. From the Planck Time to the Present, ed. S. M. Faber, 175–183

Gavazzi, G., Boselli, A., Donati, A., Franzetti, P., & Scudiego, M. 2003, A&A, 400, 451

Genel, S., Vogelsberger, M., Springel, V., et al. 2014, MNRAS, 445, 175

Graham, A. & Colless, M. 1997, MNRAS, 287, 221

Graham, M. T., Cappellari, M., Li, H., et al. 2018, MNRAS, 477, 4711

Haardt, F. & Madau, P. 1996, ApJ, 461, 20

Hayward, C. C. & Hopkins, P. F. 2016, Monthly Notices of the Royal Astronomical Society, 465, 1682

Hernández-Toledo, H. M., Vázquez-Mata, J. A., Martínez-Vázquez, L. A., Choi, Y.-Y., & Park, C. 2010, AJ, 139, 2525

Hyde, J. B. & Bernardi, M. 2009, MNRAS, 396, 1171

Kaviraj, S., Laigle, C., Kimm, T., et al. 2017, MNRAS, 467, 4739

Kennicutt, Jr., R. C. 1998, ARA&A, 36, 189

Komatsu, E., Smith, K. M., Dunkley, J., et al. 2011, ApJS, 192, 18

Kormendy, J. 2016, Galactic Bulges, 418, 431

Krumholz, M. R. & Tan, J. C. 2007, ApJ, 654, 304

Lacerna, I., Ibarra-Medel, H., Avila-Reese, V., et al. 2020, arXiv e-prints, arXiv:2001.05506

Lacerna, I., Rodríguez-Puebla, A., Avila-Reese, V., & Hernández-Toledo, H. M. 2014, ApJ, 788, 29

Lagos, C. d. P., Schaye, J., Bahé, Y., et al. 2018, MNRAS, 476, 4327

Larson, R. B. 1974, MNRAS, 169, 229

Li, H., Mao, S., Cappellari, M., et al. 2018, MNRAS, 476, 1765

Lu, S., Xu, D., Wang, Y., et al. 2020, MNRAS, 492, 5930

Ma, C.-P., Greene, J. E., McConnell, N., et al. 2014, ApJ, 795, 158

Manzano-King, C., Canalizo, G., & Sales, L. V. 2019, arXiv e-prints [arXiv:1905.09287]

Marinacci, F., Vogelsberger, M., Pakmor, R., et al. 2018, MNRAS, 480, 5113

Merloni, A. & Heinz, S. 2008, MNRAS, 388, 1011

Mo, H., van den Bosch, F. C., & White, S. 2010, Galaxy Formation and Evolution

Naab, T. 2013, in IAU Symposium, Vol. 295, The Intriguing Life of Massive Galaxies, ed. D. Thomas, A. Pasquali, & I. Ferreras, 340–349

Naiman, J. P., Pillepich, A., Springel, V., et al. 2018, MNRAS, 477, 1206

Nelson, D., Pillepich, A., Springel, V., et al. 2018, MNRAS, 475, 624

Oñorbe, J., Domínguez-Tenreiro, R., Sáiz, A., Artal, H., & Serna, A. 2006, MNRAS, 373, 503

Oñorbe, J., Domínguez-Tenreiro, R., Sáiz, A., & Serna, A. 2007, MNRAS, 376, 39

Oñorbe, J., Domínguez-Tenreiro, R., Sáiz, A., Serna, A., & Artal, H. 2005, ApJ, 632, L57

Oñorbe, J., Martínez-Serrano, F. J., Domínguez-Tenreiro, R., Knebe, A., & Serna, A. 2011, ApJ, 732, L32

Oser, L., Ostriker, J. P., Naab, T., Johansson, P. H., & Burkert, A. 2010, ApJ, 725, 2312

Pedrosa, S. E. & Tissera, P. B. 2015, A&A, 584, A43

Peirani, S., Dubois, Y., Volonteri, M., et al. 2017, MNRAS, 472, 2153

Peirani, S., Sonnenfeld, A., Gavazzi, R., et al. 2019, MNRAS, 483, 4615

Peng, Y.-j., Lilly, S. J., Kovač, K., et al. 2010, ApJ, 721, 193

Pillepich, A., Nelson, D., Hernquist, L., et al. 2018, MNRAS, 475, 648

Prugniel, P. & Simien, F. 1997, A&A, 321, 111

Prunet, S., Pichon, C., Aubert, D., et al. 2008, ApJS, 178, 179

Rasera, Y. & Teyssier, R. 2006, A&A, 445, 1

Renzini, A. & Ciotti, L. 1993, ApJ, 416, L49

Rodríguez-Gómez, V., Pillepich, A., Sales, L. V., et al. 2016, MNRAS, 458, 2371

Rosas-Guevara, Y., Bower, R. G., Schaye, J., et al. 2016, MNRAS, 462, 190

Rosito, M. S., Pedrosa, S. E., Tissera, P. B., et al. 2018, A&A, 614, A85

Rosito, M. S., Tissera, P. B., Pedrosa, S. E., & Lagos, C. D. P. 2019a, A&A, 629, L3

Rosito, M. S., Tissera, P. B., Pedrosa, S. E., & Rosas-Guevara, Y. 2019b, A&A, 629, A37

Rousseeuw, P. J. & Leroy, A. M. 1987, Robust Regression and Outlier Detection (John Wiley & Sons, Inc.)

Saglia, R. P., Bender, R., & Dressler, A. 1993, A&A, 279, 75

Salpeter, E. E. 1955, ApJ, 121, 161

Sánchez, S. F., Kennicutt, R. C., Gil de Paz, A., et al. 2012, A&A, 538, A8

Saulder, C., Mieske, S., Zeilinger, W. W., & Chilingarian, I. 2013, A&A, 557, A21

Schaye, J., Crain, R. A., Bower, R. G., et al. 2015, MNRAS, 446, 521

Sérsic, J. L. 1968, Atlas de galaxias australes

Sijacki, D., Vogelsberger, M., Genel, S., et al. 2015, MNRAS, 452, 575

Solar, M., Tissera, P. B., & Hernand ez-Jimenez, J. A. 2020, MNRAS, 491, 4894

Somerville, R. S. & Davé, R. 2015, ARA&A, 53, 51

Springel, V., Pakmor, R., Pillepich, A., et al. 2018, MNRAS, 475, 676

Starkenburg, T. K., Tonnesen, S., & Kopenhafer, C. 2019, ApJ, 874, L17

Sutherland, R. S. & Dopita, M. A. 1993, ApJS, 88, 253

Taranu, D., Dubinski, J., & Yee, H. K. C. 2015, ApJ, 803, 78

Teyssier, R. 2002, A&A, 385, 337

Tissera, P. B., White, S. D. M., & Scannapieco, C. 2012, MNRAS, 420, 255

Trujillo, I., Burkert, A., & Bell, E. F. 2004, ApJ, 600, L39

Tweed, D., Devriendt, J., Blaizot, J., Colombi, S., & Slyz, A. 2009, A&A, 506, 647

van de Sande, J., Lagos, C. D. P., Welker, C., et al. 2019, MNRAS, 484, 869

Vogelsberger, M., Genel, S., Springel, V., et al. 2014a, Nature, 509, 177

Vogelsberger, M., Genel, S., Springel, V., et al. 2014b, MNRAS, 444, 1518

Volonteri, M., Dubois, Y., Pichon, C., & Devriendt, J. 2016, MNRAS, 460, 2979

Wechsler, R. H., Bullock, J. S., Primack, J. R., Kravtsov, A. V., & Dekel, A. 2002, ApJ, 568, 52

White, S. D. M. & Frenk, C. S. 1991, ApJ, 379, 52

White, S. D. M. & Rees, M. J. 1978, MNRAS, 183, 341

Yates, R. M. & Kauffmann, G. 2014, MNRAS, 439, 3817

Zhao, D. H., Jing, Y. P., Mo, H. J., & Börner, G. 2003, ApJ, 597, L9

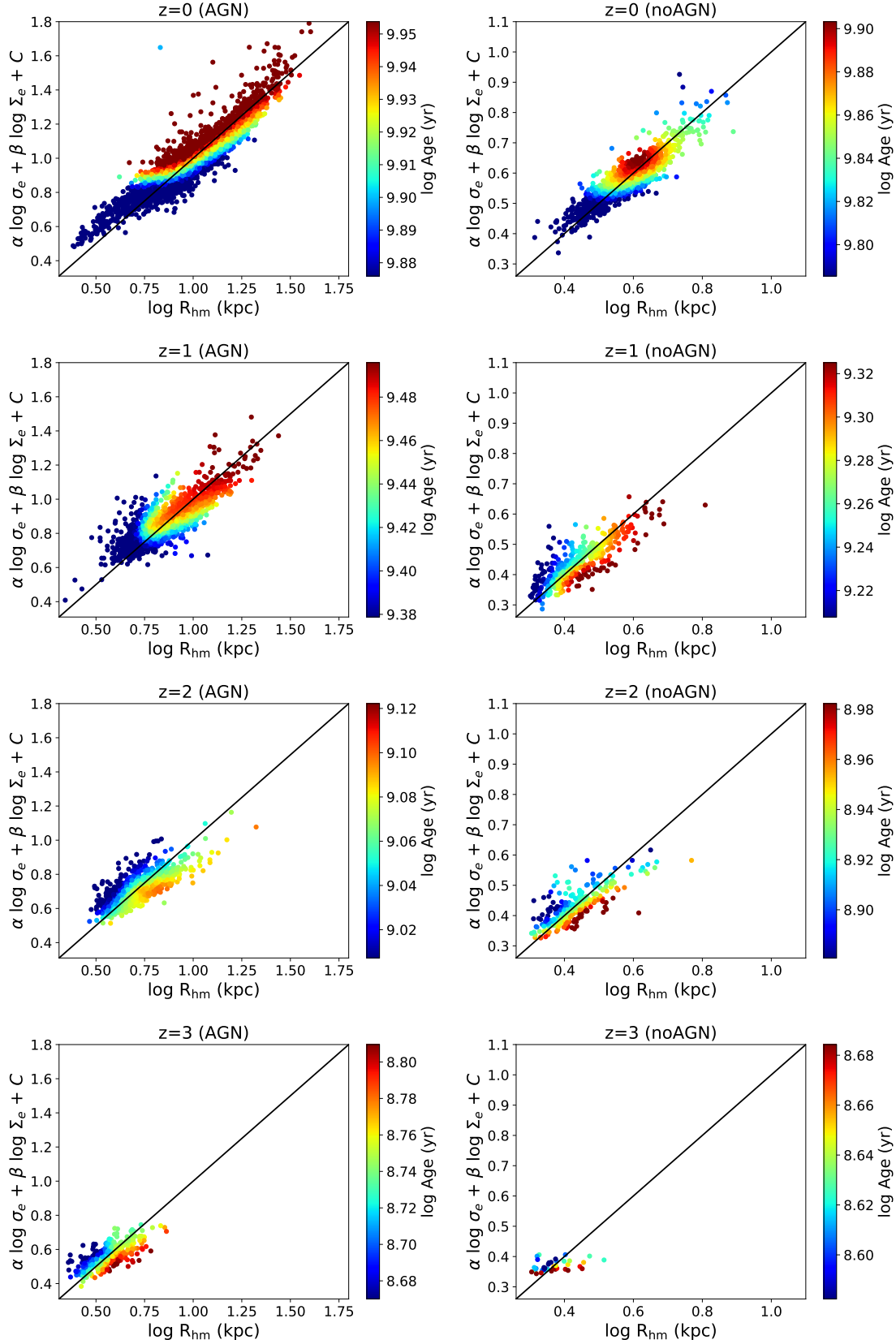


**Fig. 15.** The FP for Horizon-AGN (left panels) and Horizon-noAGN (right panels) ETGs fitted at different redshifts. The symbols are coloured according to mass-weighted average stellar age. The 1:1 line is depicted in black. In presence of AGN, we find opposite trends comparing the age distributions at  $z = 0$  and at  $z = 2$  being  $z = 1$  the time of transition. On the other hand, no clear trends are found for the Horizon-noAGN samples.

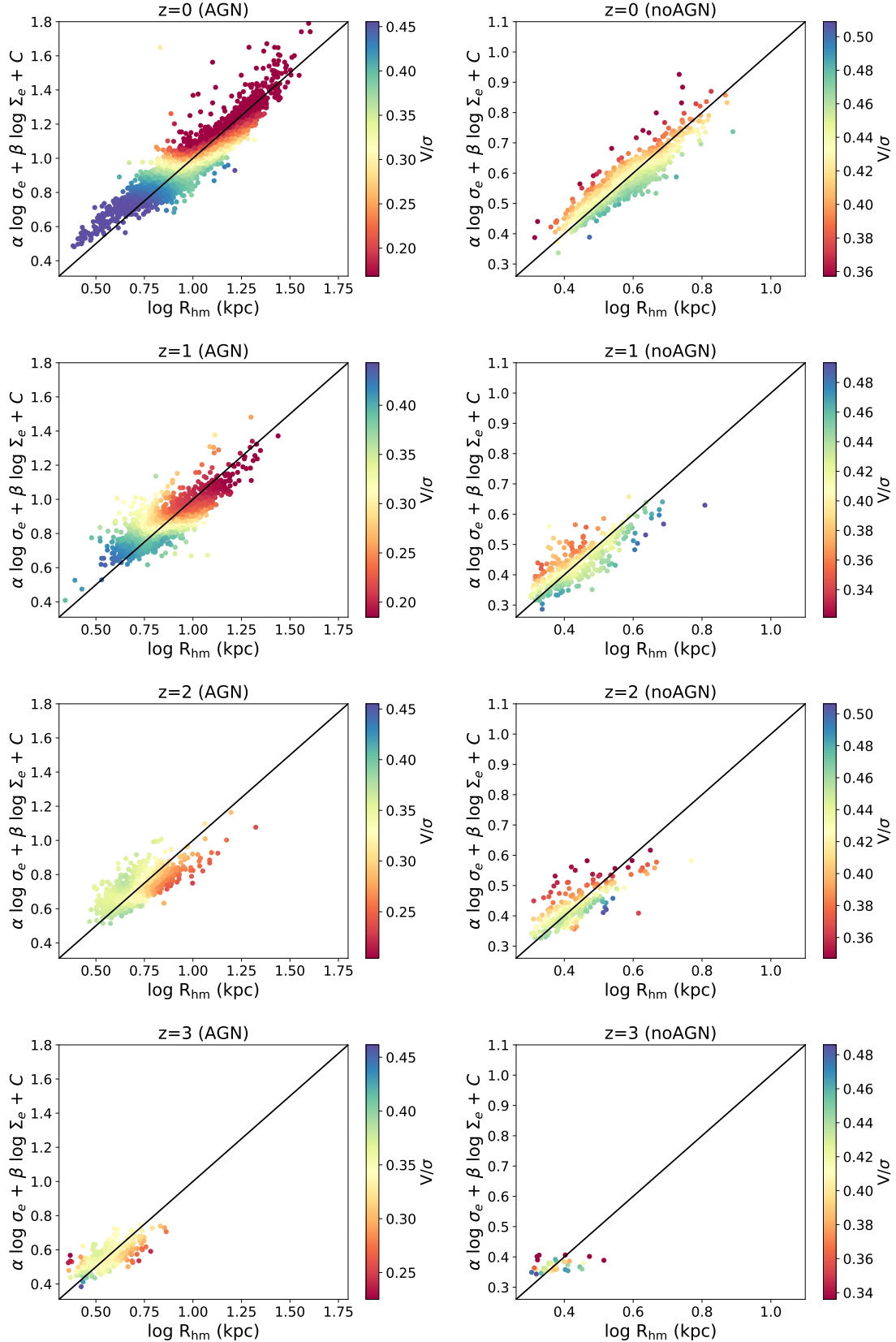


**Fig. 16.** The FP for Horizon-AGN and Horizon-noAGN (right panels) ETGs fitted at different redshifts. The symbols are coloured according to the parameter  $V/\sigma$ . The 1:1 line is depicted in black. We observe the same trends than in Fig. 15 due to the relation between age and morphology.

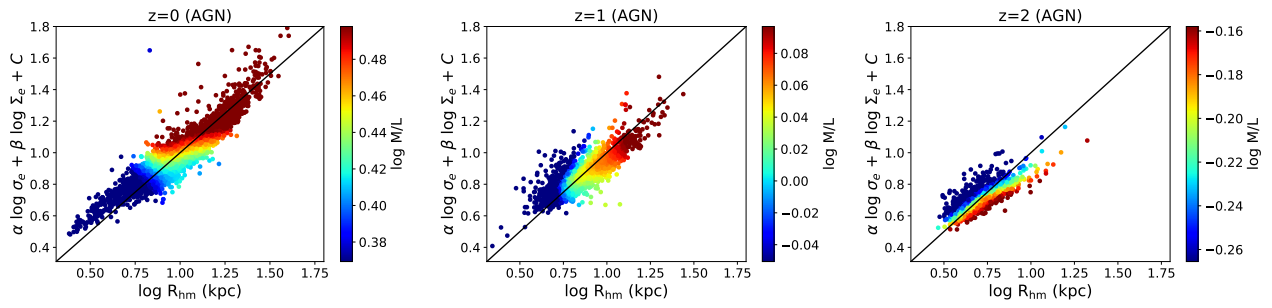


**Fig. 17.** The FP for Horizon-AGN ETGs as a function of  $M/L$  at  $z = 0, 1$  and  $z = 2$ .

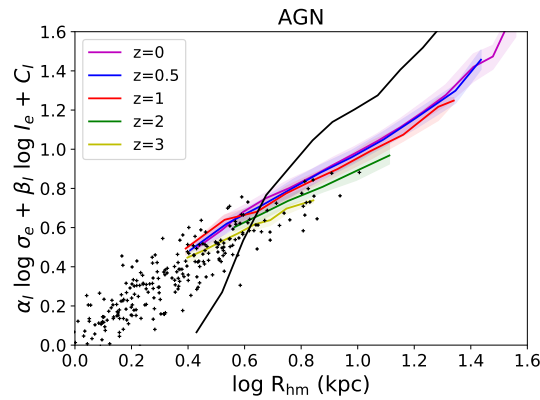


**Fig. 18.** The L-FP for Horizon-AGN sample computing the average surface brightness for both observations (Cappellari et al. 2013a) and simulation, using the luminosity in the r-band.

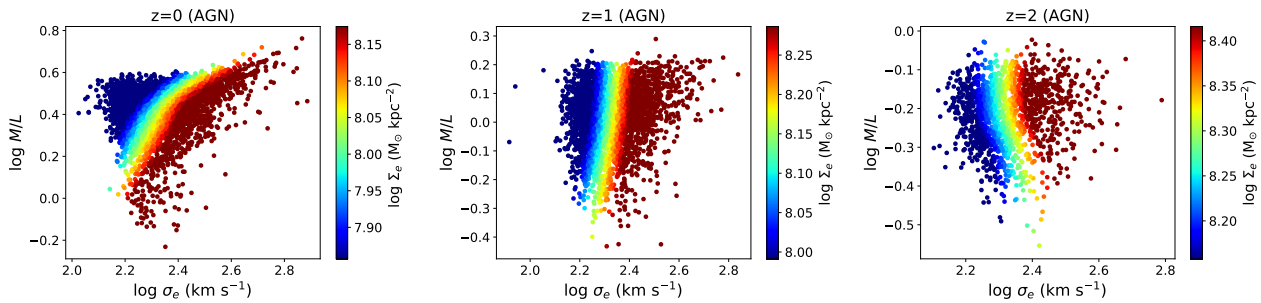


**Fig. 19.** Relation between  $M/L$  ratio and velocity dispersion for Horizon-AGN ETGs at  $z = 0, 1$  and  $z = 2$ . Symbols are coloured by the average surface density  $\Sigma_e$ .

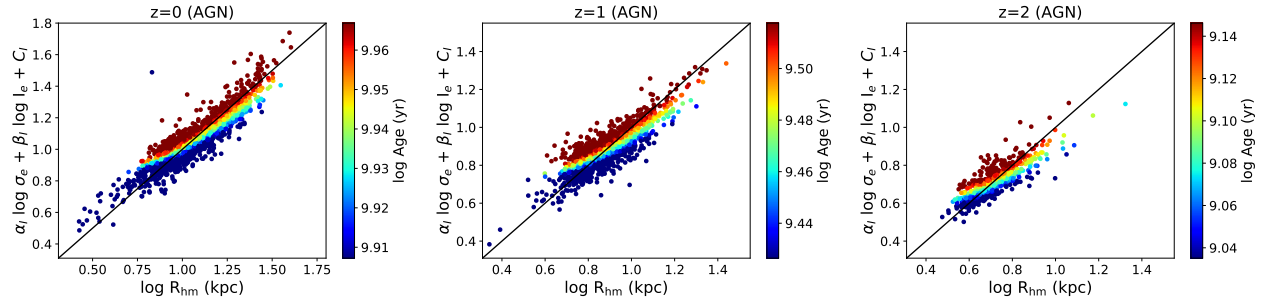


**Fig. 20.** The L-FP for Horizon-AGN ETGs fitted at different redshifts where ETGs are defined as the ones with  $V/\sigma < 0.3$ . The symbols are coloured according to mass-weighted stellar ages. The 1:1 line is depicted in black.

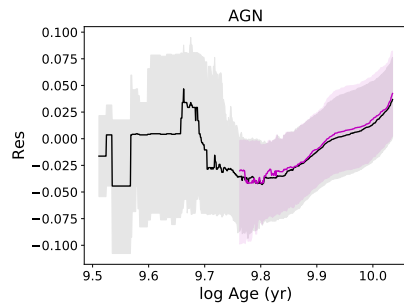


**Fig. 21.** The residuals of the L-FP at  $z = 0$  with the restriction  $V/\sigma < 0.3$  as a function of mass weighted average age (black line). We depict the residuals of the subsample of passive galaxies (defined by Lacerna et al. 2014) in magenta lines. The regions between the 25 and 75 percentiles are shaded.

## Appendix A: Non-smoothed plots

Due to the fact that the method implemented to obtain smooth distributions in scatter plots coloured by a third variable can mislead the interpretation of the real trends, we include in this Appendix the non-smoothed version of those plots.

## Appendix B: Morphological classification

In this work, we apply the criterion in Chisari et al. (2015) to morphologically classify galaxies in ETGs and LTGs. In this Appendix, we verify the consistency of this criterion with that used by Rosito et al. (2018, 2019a) and Rosito et al. (2019b), in which galaxies are classified by using the  $B/T$  ratio following the method described in Tissera et al. (2012), being  $B/T = 0.5$  the adopted threshold for a galaxy to be considered spheroid dominated.

We measure quantitatively the amount of rotation in the analysed samples. For this purpose, we calculate a parameter  $\sigma/V$  for each particle within  $R_{\text{opt}}$ . We define the dispersion locally by taking radial bins around the centre of a galaxy in which we calculate the average of each velocity component. Thus,  $\sigma$  for each particle is calculated relative to that averages and  $V$  is the particle tangential velocity. If  $0 < \sigma/V < 1$ , that particle is considered part of the disc and thus, we are able to calculate disc-to-total stellar mass ratio ( $D/T$ ), which may play the role of  $B/T$  in the works mentioned above. In Fig. B.1 we show the distribution of this parameter for an individual ETG from Horizon-AGN simulation. It is clear that there is no counter-disc and that the galaxy is dominated by velocity dispersion.

As regards the comparison between  $D/T$  calculated as described above and the global parameter  $V/\sigma$  (Dubois et al. 2014) utilised for the classification in this work, we find an excellent correlation between them, with a p-value of the Spearman coefficient near 0 in the selected sample of Horizon-AGN (see Fig B.2). Therefore, we conclude the consistency between both classifications.

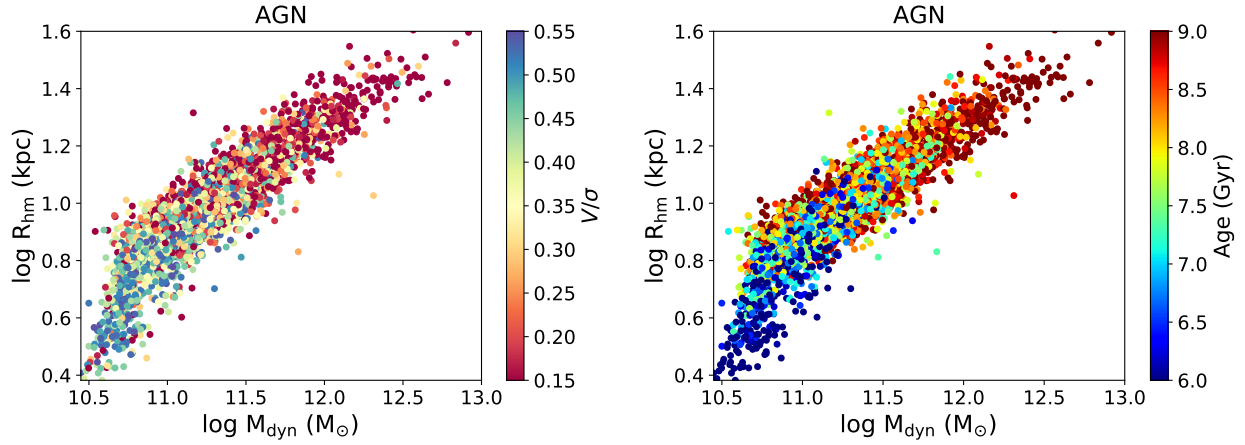


**Fig. A.1.** Mass-size plane as a function of  $V/\sigma$  (left panel) and mass-weighted average stellar age (right panel) for the Horizon-AGN sample of ETGs. See Fig. 5 for the smoothed version.

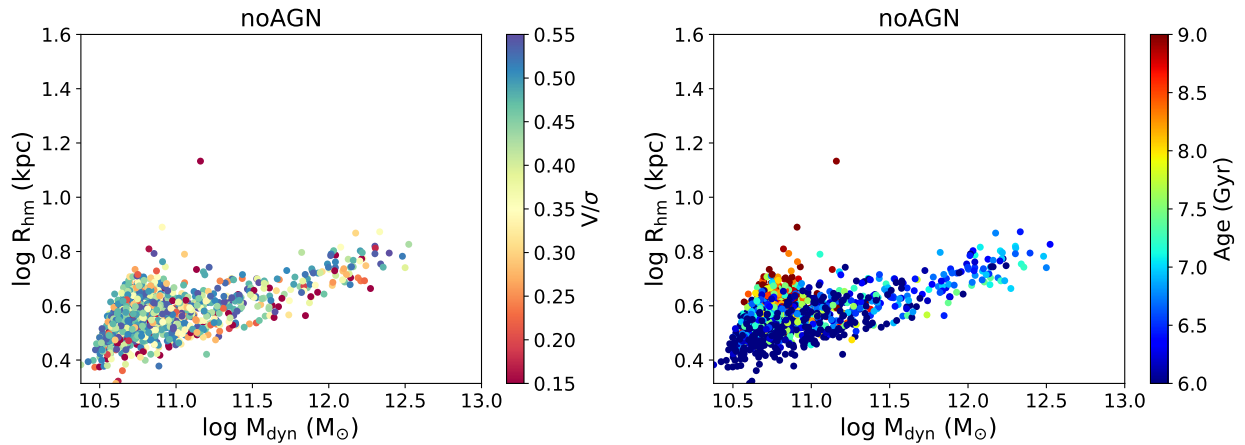


**Fig. A.2.** Mass-size plane as a function of  $V/\sigma$  (left panel) and mass-weighted average stellar age (right panel) for the Horizon-noAGN sample of ETGs. See Fig. 6 for the smoothed version.

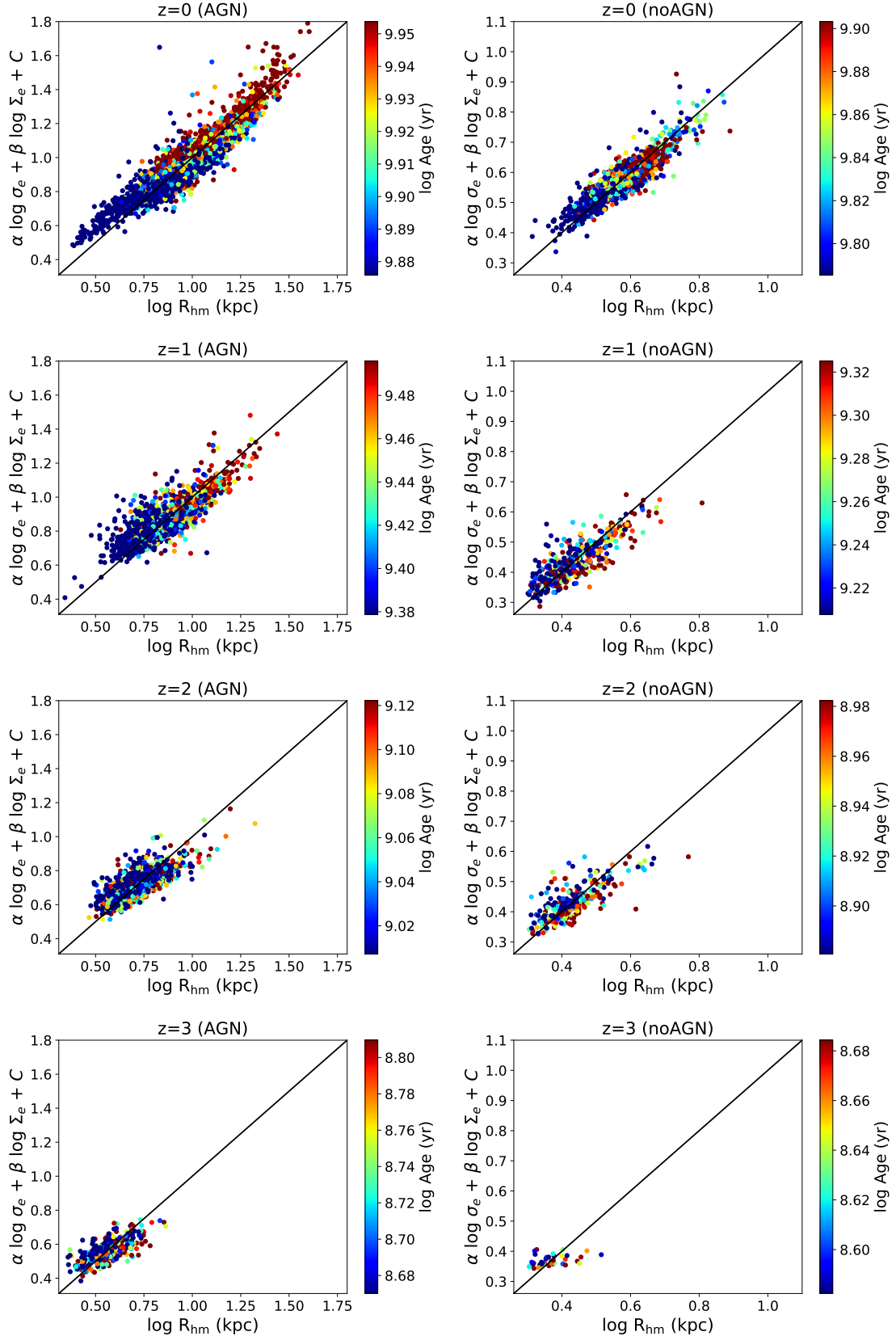


**Fig. A.3.** The FP for Horizon-AGN (left panels) and Horizon-noAGN (right panels) ETGs fitted at different redshifts. The symbols are coloured according to mass-weighted stellar ages. The 1:1 line is depicted in black. See Fig. 15 for the smoothed version.

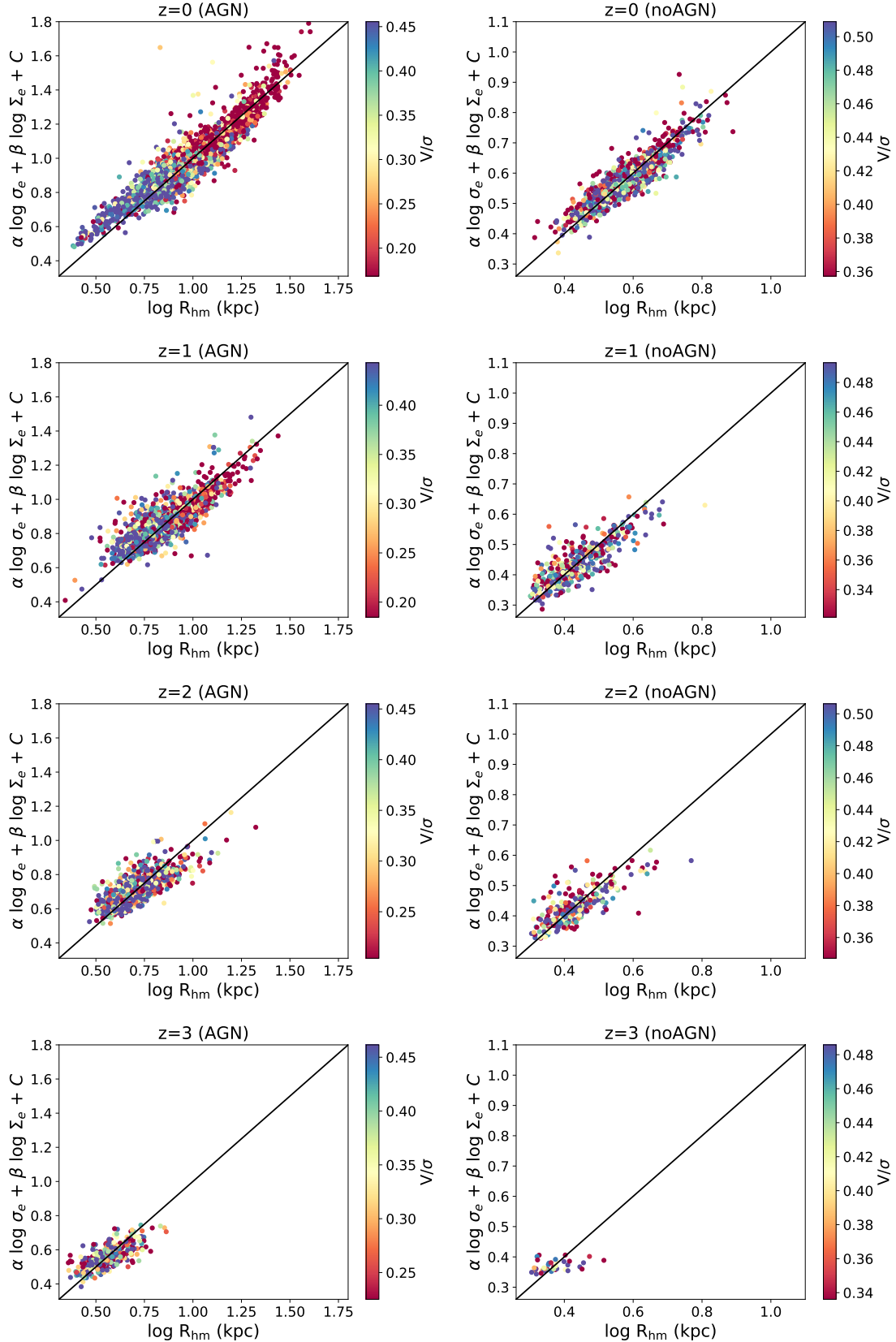


**Fig. A.4.** The FP for Horizon-AGN and Horizon-noAGN (right panels) ETGs fitted at different redshifts. The symbols are coloured according to the parameter  $V/\sigma$ . The 1:1 line is depicted in black. See Fig. 16 for the smoothed version.

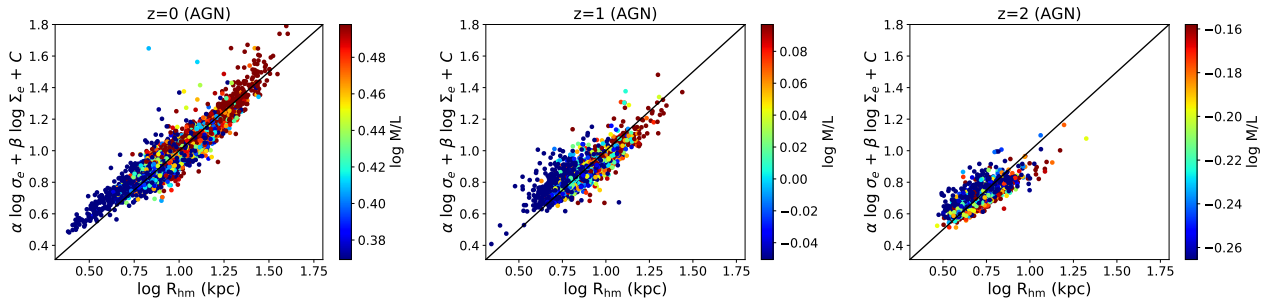


**Fig. A.5.** The FP for Horizon-AGN ETGs as a function of  $M/L$  at  $z = 0, 1$  and  $z = 2$ . See Fig. 17 for the smoothed version.

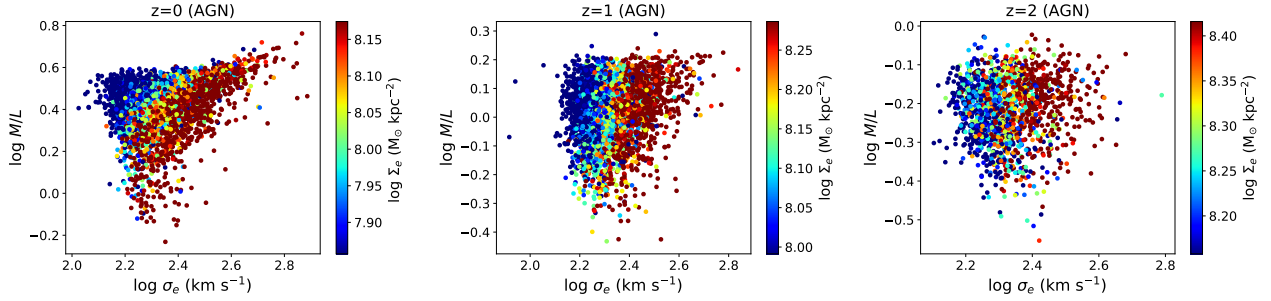


**Fig. A.6.** Relation between  $M/L$  ratio and velocity dispersion for Horizon-AGN ETGs at  $z = 0, 1$  and  $z = 2$ . Symbols are coloured by the average surface density  $\Sigma_e$ . See Fig. 19 for the smoothed version.

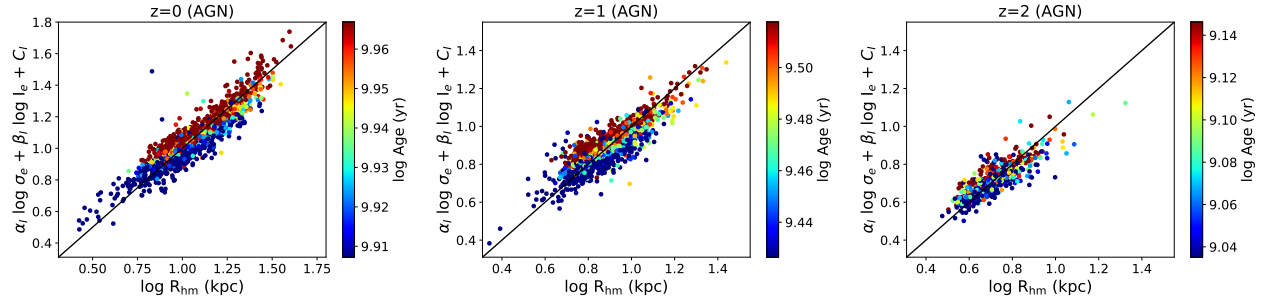


**Fig. A.7.** The L-FP for Horizon-AGN ETGs fitted at different redshifts where ETGs are defined as the ones with  $V/\sigma < 0.3$ . The symbols are coloured according to mass-weighted stellar ages. The 1:1 line is depicted in black. See Fig. 20 for the smoothed version.

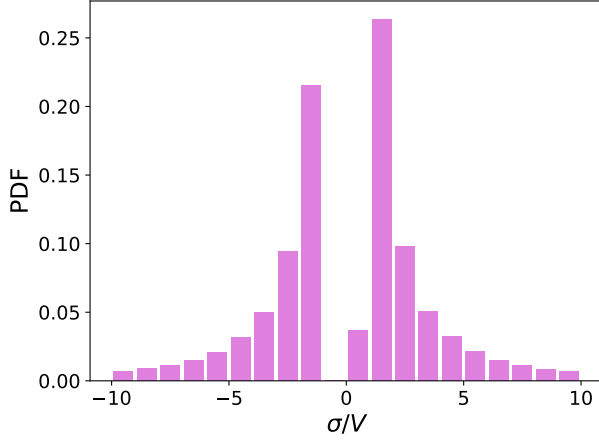


**Fig. B.1.** Distribution of  $\sigma/V$  estimated for each stellar particles for a typical ETG selected from the Horizon-AGN simulation.

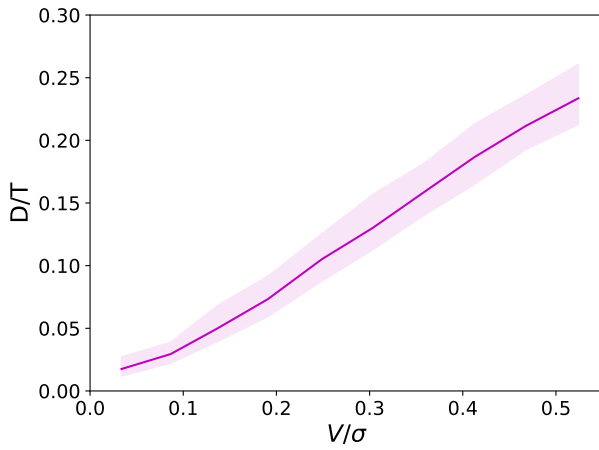


**Fig. B.2.**  $D/T$  as a function of  $V/\sigma$  for ETGs from Horizon-AGN simulation. The remarkable correlation (p-value  $\sim 0$ ) between them verify the consistency of our morphological classification and the one presented in Rosito et al. (2018).